Buoyancy-Driven Fluid Dynamics for Enhanced Ocular Drug Delivery

Thesis by
Stephanie O'Gara

In Partial Fulfillment of the Requirements for the
Degree of
PhD in Mechanical Engineering

CALIFORNIA INSTITUTE OF TECHNOLOGY
Pasadena, California

2025
Defended April 14, 2025

Stephanie O'Gara
ORCID: 0009-0003-9826-6906

ACKNOWLEDGEMENTS

This thesis would not have been possible without the support of countless people. Firstly, I would like to extend my deepest gratitude to my advisor, Prof. Mory Gharib. His knowledge and enthusiasm for fluid dynamics and all its interesting applications continuously inspired me, and his openness to new ideas allowed me to think creatively. I would like to thank Prof. Manoochehr Koochesfahani, who I had the pleasure of collaborating with on the second chapter of this thesis. He challenged me to pay closer attention to the details which helped me grow as a researcher. I would like to extend my gratitude to the other members of my thesis committee, Prof. John Dabiri, Prof. Ruby Fu, and Dr. Mark Humayun, for their careful review and feedback on this thesis.

I would like to thank Dr. David Jeon for his guidance and patience with answering my many questions on the flow imaging techniques detailed in the third chapter of this thesis. I am grateful to my collaborator, Noah Van Santan, for his contributions to the sixth chapter of this thesis. I would like to thank my lab mates for their thoughtful questions and discussions on my work.

To the friends who added warmth and color to my life outside of lab: you are the reason I made it through. Thank you to my friends near and far, especially Tracy, Eric, Sorina, and Sahangi. I cherish the community we created together.

This thesis would not have been possible without my family. I always knew who to turn to for encouragement during setbacks and who to celebrate my wins with. Their unconditional love and support kept me going. I am forever thankful for my mom and dad, Clotilde and Bill, and my siblings, Ali, Katie, and Billy.

Lastly, I would like to dedicate this thesis to my nieces and nephew, Natalia, Cecilia, and Luke. Watching you grow over the past few years has been my greatest joy, and missing you from California made me work faster to finish this thesis.

Financial support for this work came from the Cross-Resnick First Year Fellowship and the National Science Foundation Graduate Research Fellowship under Grant No. DGE-1745301.

ABSTRACT

The CDC has identified vision loss as a growing public health concern, with eye disease prevalence on the rise. Three of the most common and vision-threatening eye diseases, wet age-related macular degeneration, proliferative diabetic retinopathy, and diabetic macular edema, are typically managed through periodic intravitreal injections. However, treatment effectiveness varies. Given that the half-life of the drug is limited, one possible cause of the ineffective treatment is inefficient delivery to the target region. This thesis investigates heat-induced convective flow in an in-vitro eye model as a method for enhancing drug delivery by accelerating fluid transport.

First, an optical distortion study was conducted to identify a vitreous model that matches both the viscosity of the human vitreous and the refractive index of the eye model. Next planar two-component and volumetric three-component flow visualization and measurement experiments capture the impact of thermal pad size on the resulting flow fields, with consideration given to particle trajectories for targeted delivery. Finally, a physics-informed neural network, trained on planar velocity data and tested against additional planes from volumetric measurements, demonstrates the potential for data-driven modeling to simplify future flow visualization experiments. The outcomes of this work further our fundamental understanding of fluid dynamics in the eye and encourage continued investigation into interdisciplinary approaches for improving drug delivery, and ultimately, patient outcomes.

PUBLISHED CONTENT AND CONTRIBUTIONS

[1] S. O'Gara, M. Koochesfahani, and M. Gharib, "Index matching for quantitative measurements in an in-vitro vitreous eye model," in preparation. O'Gara performed the experiments, analyzed the data, and prepared the manuscript.

[2] S. O'Gara, N. Van Santan, and M. Gharib, "Physics-informed neural network for experimental buoyancy-driven flow," in preparation.
O'Gara conceptualized the project, performed the experiments, analyzed the data, developed the PINN framework, and prepared the manuscript.

TABLE OF CONTENTS

LIST OF ILLUSTRATIONS

Number *Page*

LIST OF TABLES

Chapter 1

INTRODUCTION

1.1 Background and Motivation

Eye Anatomy

The eye is a delicate, complex structure, and the precise fluid systems in the eye are critical to maintaining its health. At a fundamental level, the human eye is organized into three primary layers, each with specialized functions. The outer fibrous layer, which includes the tough sclera and the transparent cornea, provides structural support. Beneath this is the middle vascular layer, comprising the iris, ciliary body, and choroid, which delivers essential nutrients while removing metabolic waste. The innermost layer, the retina, is a sophisticated neural tissue that converts light into electrical signals, which are sent to the brain for processing. Within the retina lies the macula, a specialized region that is critical for sharp, detailed central vision due to its high concentration of photoreceptors [2], [3].

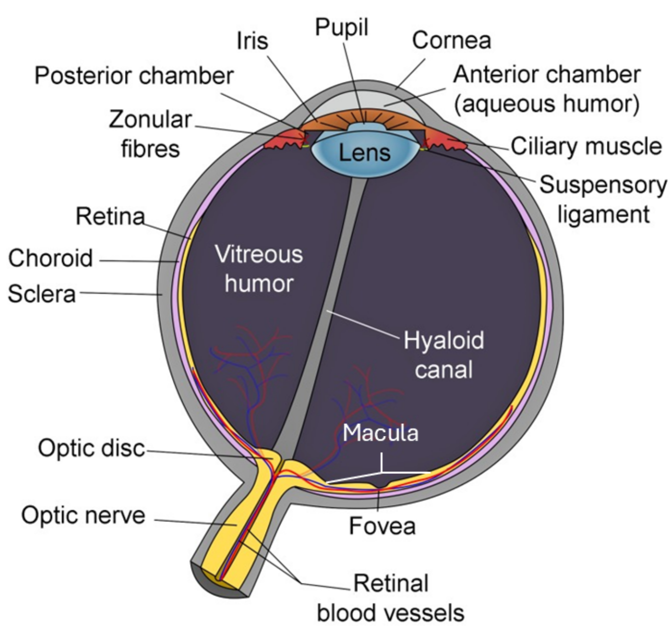

Figure 1.1: Schematic diagram of the human eye, illustrating key anatomical components including the choroid, retina, optic nerve, vitreous humor, and macula (adapted from [1]).

In addition to these layers, the eye contains three chambers that are critical for maintaining intraocular pressure and ensuring proper metabolic exchange. The anterior chamber, located between the cornea and the iris, is filled with aqueous humor, which nourishes the cornea and lens. Aqueous humor is continuously produced in the narrow posterior chamber, situated between the iris and the lens, where it flows forward through the pupil [2]. Behind the lens, the vitreous chamber, the largest of the three chambers, is filled with vitreous humor, a gel-like substance that ensures stable intraocular metabolism and function [4]. Together, these layers and chambers enable the eye to perform complex visual tasks while safeguarding its delicate structures.

Eye Diseases

The CDC has identified vision loss as a growing public health concern [5], [6]. In 2015 in the US, 1.02 million people were blind, 3.22 million people had visual impairment, and 8.2 million people had vision problems due to uncorrected refractive error [7]. These figures are projected to double by 2050, driven largely by a rapidly aging population and the growing epidemic of diabetes [7]. Among the most common and severe ocular diseases are age-related macular degeneration (AMD) and diabetic retinopathy (DR). AMD predominantly affects older adults, while DR—particularly in its most damaging forms, proliferative diabetic retinopathy (PDR) and diabetic macular edema (DME)—has surged due to the rising prevalence of diabetes. These conditions impact millions globally (Table 1.1) and represent critical targets for further research and intervention.

	Global Prevalence (2020)	Global Projection
AMD	196 million	288 million (2040)
Diabetic Retinopathy	103.12 million	160.50 million (2045)
Blindness	43.3 million	61.0 million (2050)
Moderate and Severe Vision Impairment	295 million	474 million (2050)

Table 1.1: Global prevalence and projections for age-related macular degeneration and diabetic retinopathy, as well as blindness and vision impairment more generally, highlighting the anticipated rise in cases over the coming decades and the growing public health burden associated with these vision-threatening conditions. Sources for AMD and diabetic retinopathy data are [8] and [9], respectively. Data on blindness and vision impairment is from [10].

.

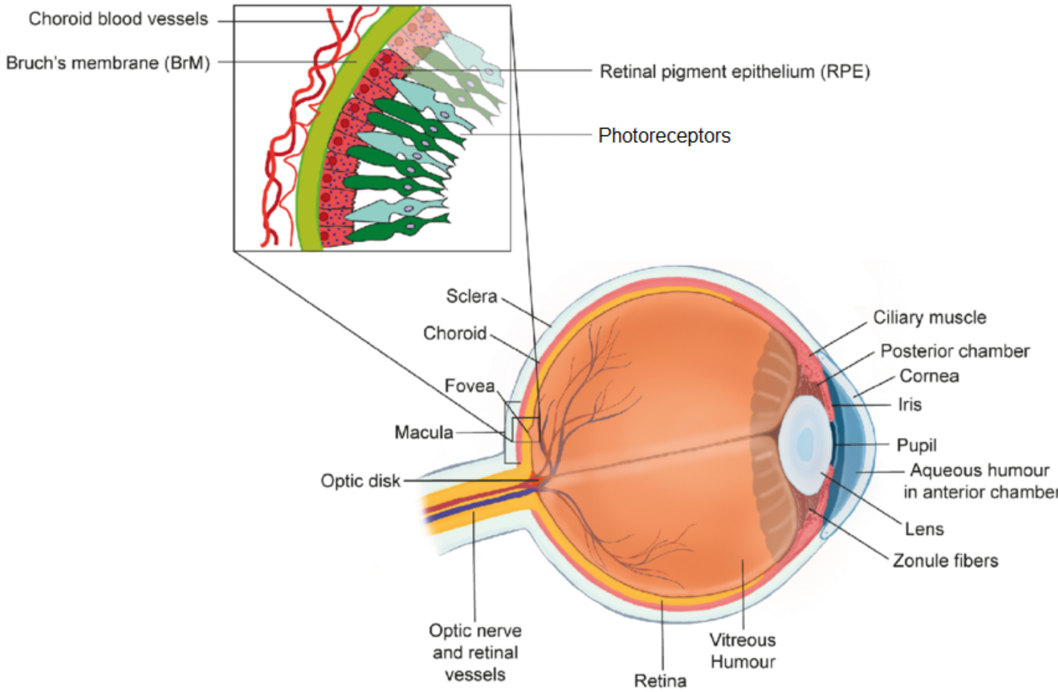

Figure 1.2: Anatomy of the human eye, highlighting the Bruch's membrane and its relationship to surrounding structures, including the choroid blood vessels, retinal pigment epithelium, and photoreceptor cells (adapted from [11]).

Age-related macular degeneration is the third leading cause of visual impairment worldwide [12]. Projections estimate that 288 million people will have AMD by 2040 [8]. There are two forms of AMD, wet and dry, where wet AMD is more severe and accounts for about 20% of all AMD patients [13]. Dry AMD is characterized by a thickening of the Bruch's membrane, due to lipid and protein accumulation, leading to the formation of subretinal pigment epithelium deposits [14]. These deposits can impede the exchange of nutrients and waste products between the retina and the choroid, leading to retinal damage [14], [15]. Visual loss from dry AMD occurs slowly over years [16]. Patients with dry AMD are monitored for progression to wet AMD. In wet AMD, abnormal, fragile blood vessels from the choroid grow through defects in the Bruch's membrane into the subretinal space. These neovessels are prone to leaking fluid and blood, leading to fluid accumulation, swelling, and localized hemorrhages, which can damage the macula. Vision loss occurs rapidly, over the course of days or weeks [16].

Diabetic retinopathy is a vision-threatening complication of diabetes. The elevated glucose levels, or hyperglycemia, in patients with diabetes damages blood vessels throughout the body, including in the eye. Like AMD, there are two stages of disease progression. Non-proliferative diabetic retinopathy is the early stage, characterized by weakened blood vessels in the retina. Proliferative diabetic retinopathy is the advanced stage, characterized by neovascularization in response to reduced blood flow. Like wet AMD, these neovessels are prone to leakage and bleeding, and often originate around the optic disk at the back of the eye [17]. This can result in vitreous hemorrhage and retinal detachment, leading to severe vision loss.

Diabetic macular edema is a major complication of diabetic retinopathy and can occur at any stage of DR. In DME, chronic hyperglycemia damages the retinal blood vessels, leading to leakage of fluid into the macula. This accumulation of fluid causes the macula to swell and thicken. DME can cause distortion of visual images and a decrease in visual acuity. Untreated, it can lead to total loss of vision [17].

Intravitreal Injections

Periodic intravitreal injections of anti-vascular endothelial growth factor (anti-VEGF) have become a cornerstone in managing wet AMD, PDR, and DME. Anti-VEGF injections work by blocking vascular endothelial growth factor, a protein that promotes the growth of abnormal blood vessels and increases vascular permeability. In wet AMD and PDR, these injections inhibit the abnormal growth of fragile, leaky blood vessels. Similarly, in DME, these injections help prevent the leakage of fluid from damaged vessels. Anti-VEGF injections can be effective at stabilizing (9 in 10) and improving visual acuity (1 in 3) in patients [18].

For the treatment, an ophthalmologist injects 50 microliters of anti-VEGF into the patient's vitreous chamber using a 30-gauge needle [19]. Approximately four weeks after the injection, the ophthalmologist assesses the patient's visual acuity to determine the treatment's effectiveness and to decide if additional injections are necessary or if a follow-up can be scheduled for a later date [20]. This periodic assessment is crucial for monitoring disease progression and optimizing therapeutic outcomes.

While intravitreal injections are generally well-tolerated, there are potential complications. Mild side effects may include transient increases in intraocular pressure and ocular inflammation. Examples of more serious, albeit rare, complications include retinal detachment, ocular hemorrhage, and endophthalmitis, a vision-threatening infection [21]. Many patients cease anti-VEGF treatments [22], despite the risk for severe vision loss, due to a number

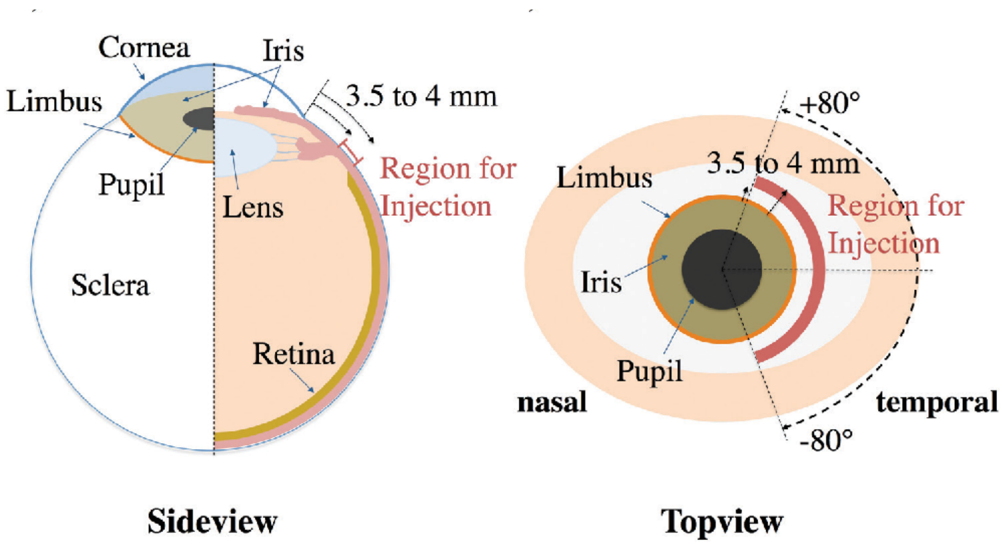

Figure 1.3: The safe region for intravitreal injection spans between ± 80° from the horizontal with a radial distance of 3.5mm to 4mm from the limbus [24].

of factors, including cost, inconvenience, discomfort/pain, and poor response to treatment [23].

While wet AMD, PDR, and DME can usually be managed through periodic intravitreal injections of anti-VEGF, the treatment effectiveness varies, and drug delivery across the vitreous chamber remains difficult. One contributing factor is the significant variation in ocular anatomy among patients and the differences in injection techniques among ophthalmologists. The diameter of the human eye typically ranges from 2.1 to 2.7cm, with an average of 2.42cm [25]. The standard injection site, 3.5 to 4mm posterior to the limbus, spans a wide area [19], as illustrated in Figure 1.3. These variables can result in inconsistencies in treatment.

Delivering anti-VEGF agents is further complicated by the need for the drug to traverse the vitreous chamber and penetrate multiple cellular layers. The outer and inner blood–retinal barriers are formed by tight junctions between retinal pigment epithelial cells and retinal endothelial cells, respectively [26]–[28]. Together, these barriers hinder drug penetration to the damaged blood vessels within the retina.

Another challenge is that the half-life of the anti-VEGF agents is limited, and the timescale to cross the vitreous chamber by pure diffusion varies greatly, depending on patient anatomy and size of the anti-VEGF molecules.

The three most popular anti-VEGF agents are bevacizumab (brand name: Avastin), aflibercept (brand name: Eylea), and ranibizumab (brand name: Lucentis) [29].

The diffusion coefficients for ranibizumab and bevacizumab are estimated to be $1.34 \times 10^{-6}\,\mathrm{cm}^2/\mathrm{s}$ in a physiological saline and $(1.2 \pm 0.6) \times 10^{-6}\,\mathrm{cm}^2/\mathrm{s}$ in a rabbit vitreous, respectively [30], [31]. The hydrodynamic radii for ranibizumab, aflibercept, and bevacizumab were measured to be 2.76 ± 0.04, 3.70 ± 0.03, and 4.58 ± 0.01nm, respectively [32]; therefore, we estimate that the diffusion coefficient for aflibercept is within the range of ranibizumab and bevacizumab.

To estimate the timescale to cross the vitreous chamber, we look to Fick's second law of diffusion, which states that the time rate of change in concentration (at x and t) is proportional to the curvature of the concentration function (at x and t), scaled by the diffusion coefficient [33]:

$$\frac{\partial \varphi}{\partial t} = D \frac{\partial^2 \varphi}{\partial x^2} \tag{1.1}$$

where:

- φ = Concentration
- t = Time
- D = Diffusion coefficient
- x = Position.

For an order-of-magnitude estimate, we can approximate the timescale for diffusion as:

$$t \approx \frac{L^2}{D} \tag{1.2}$$

where:

- t = Timescale for diffusion (s)
- D = Diffusion coefficient (cm^2/s)
- L = Diameter of the eye (cm).

While the intravitreal injection may occur some depth into the vitreous chamber, we use the average eye diameter as a representative length scale to estimate the average upper bound on the timescale for diffusion. Using Equation 1.2, the timescale for diffusion across the vitreous is approximately 50 days. In human eyes, the aqueous half-life of intravitreally injected ranibizumab, bevacizumab, and aflibercept is 7.19, 9.82, and 11 days, respectively [34]–[36]. Therefore, for patients who are not improving with intravitreal anti-VEGF injections, inefficient drug delivery could be one cause. Consequently, innovative strategies are needed to enhance drug transport, ensuring that the drug reaches the target area more quickly.

One possible solution is to induce advective mass transport, which could accelerate the movement of the injected drug within the eye. Enhancing fluid mixing in the vitreous and optimizing drug delivery could potentially improve treatment outcomes for patients.

Furthermore, if treatment effectiveness is improved, it may allow for longer-lasting treatment effects, potentially reducing the frequency of injections needed. This would have considerable benefits, including lowering total treatment costs, reducing patient inconvenience, and minimizing risks and complications associated with repeated intravitreal injections.

Previous Research Efforts

It is worth noting that there have not been many studies on the role of convection in promoting drug distribution in the eye [37]. Groups have examined how eye rotations induce convection for drug transport both experimentally [38]–[41] and computationally [42]–[45]. However, rapid eye movements may be unpleasant after an injection, and the overall circulation effects induced by lateral movements do not sustain for long enough to ensure thorough drug distribution [39].

Another strategy for inducing advective mass transport is applying heat to the eye. [46] performed dye visualization experiments with injections into a glass eye model to compare the dye concentration by pure diffusion and convection-assisted transport. For the convection-assisted case, they mimicked laser irradiation on the retinal surface by embedding a heater on the retinal surface of the glass eye. The desired concentration (12.95 g/mL at the target region) was reached in 12 minutes compared to 12 hours by pure diffusion. [47] showed, through dye visualization and two-component planar particle image velocimetry experiments, that applying a thermal load induces strong circulation in an eye model. They also investigated how different heating positions and heater temperatures affect mixing. This study was the first to demonstrate that heat addition can induce circulation in an eye model; however, the limited two-component PIV measurements, taken only at the center plane, do not capture the full flow behavior throughout the entire eye model.

Filling this gap in the literature, this thesis investigates the two and three-dimensional fluid dynamics of heat-assisted convection within an in-vitro eye model, focusing on its application to intravitreal drug delivery.

1.2 Organization of this Thesis

The second chapter of the thesis focuses on the vitreous humor and the technique we employed to identify a vitreous model that matched both the viscosity in the human vitreous and the refractive index of the eye model. The third chapter details the experimental setups and software used for planar two-component particle image velocimetry and volumetric three-component particle tracking velocimetry. In the fourth chapter, we examine the effects of thermal pad size variation on the resulting flow field and particle trajectories. In the sixth chapter, we investigate, using our experimental data, whether a physics-informed neural network, trained on data acquired through planar experimental techniques, can predict additional planes from a volumetric flow field. Finally, the seventh chapter concludes this study and discusses avenues for future work.

Chapter References

[1] A. Omari and T. H. Mahmoud, "Vitrectomy," in *StatPearls*, Treasure Island (FL): StatPearls Publishing, 2025.

[2] T. Root, "OphthoBook." CreateSpace Independent Publishing Platform, Jul. 20, 2009.

[3] E. S. Perkins and H. Davson, "Human eye," in *Encyclopedia Britannica*, Feb. 10, 2025.

[4] Y. Zong, Q.-Y. Gao, and Y.-N. Hui, "Vitreous function and intervention of it with vitrectomy and other modalities," *International Journal of Ophthalmology*, vol. 15, no. 6, pp. 857–867, Jun. 18, 2022. DOI: `10.18240/ijo.2022.06.02`.

[5] CDC. "Why vision loss is a public health problem," Vision and Eye Health. (May 24, 2024).

[6] J. B. Saaddine, K. Venkat Narayan, and F. Vinicor, "Vision loss: A public health problem?" *Ophthalmology*, vol. 110, no. 2, pp. 253–254, Feb. 1, 2003. DOI: `10.1016/S0161-6420(02)01839-0`.

[7] R. Varma, T. S. Vajaranant, B. Burkemper, *et al.*, "Visual impairment and blindness in adults in the United States: Demographic and geographic variations from 2015 to 2050," *JAMA Ophthalmology*, vol. 134, pp. 802–809, 7 Jul. 2016. DOI: `10.1001/jamaophthalmol.2016.1284`.

[8] W. L. Wong, X. Su, X. Li, *et al.*, "Global prevalence of age-related macular degeneration and disease burden projection for 2020 and 2040: A systematic review and meta-analysis," *The Lancet Global Health*, vol. 2, no. 2, e106–116, Feb. 2014. DOI: `10.1016/S2214-109X(13)70145-1`.

[9] Z. L. Teo, Y.-C. Tham, M. Yu, *et al.*, "Global prevalence of diabetic retinopathy and projection of burden through 2045: Systematic review and meta-analysis," *Ophthalmology*, vol. 128, no. 11, pp. 1580–1591, Nov. 2021. DOI: `10.1016/j.ophtha.2021.04.027`.

[10] R. Bourne, J. D. Steinmetz, S. Flaxman, *et al.*, "Trends in prevalence of blindness and distance and near vision impairment over 30 years: An analysis for the global burden of disease study," *The Lancet Global Health*, vol. 9, no. 2, e130–143, Feb. 1, 2021. DOI: `10.1016/S2214-109X(20)30425-3`.

[11] J. Betts and L. Troeberg, "Review: Mechanisms of TIMP-3 accumulation and pathogenesis in sorsby fundus dystrophy," *Molecular Vision*, vol. 30, pp. 74–91, Mar. 2024.

[12] M. Chaudhuri, Y. Hassan, P. P. S. Bakka Vemana, M. S. Bellary Pattanashetty, Z. U. Abdin, and H. F. Siddiqui, "Age-related macular degeneration: An exponentially emerging imminent threat of visual impairment and irreversible blindness," *Cureus*, vol. 15, no. 5, DOI: `10.7759/cureus.39624`.

[13] K. Boyd. “Understanding macular degeneration,” American Academy of Ophthalmology. (Oct. 1, 2024).

[14] A. Pugazhendhi, M. Hubbell, P. Jairam, and B. Ambati, “Neovascular macular degeneration: A review of etiology, risk factors, and recent advances in research and therapy,” *International Journal of Molecular Sciences*, vol. 22, no. 3, p. 1170, Jan. 25, 2021. DOI: 10.3390/ijms22031170.

[15] H. R. Coleman, C.-C. Chan, F. L. Ferris, and E. Y. Chew, “Age-related macular degeneration,” *Lancet*, vol. 372, no. 9652, pp. 1835–1845, Nov. 22, 2008. DOI: 10.1016/S0140-6736(08)61759-6.

[16] S. Mehta. “Age-related macular degeneration (AMD or ARMD) - eye disorders,” Merck Manual Professional Edition. (Apr. 2024).

[17] W. Crasto, V. Patel, M. J. Davies, and K. Khunti, “Prevention of microvascular complications of diabetes,” *Endocrinology and Metabolism Clinics of North America*, vol. 50, no. 3, pp. 431–455, Sep. 2021. DOI: 10.1016/j.ecl.2021.05.005.

[18] J. Evans and G. Virgili, “Anti-VEGF drugs: Evidence for effectiveness,” *Community Eye Health*, vol. 27, no. 87, p. 48, Jan. 1, 2014.

[19] D. Yorston, “Intravitreal injection technique,” *Community Eye Health*, vol. 27, no. 87, p. 47, 2014.

[20] P. V. Algvere, B. Steén, S. Seregard, and A. Kvanta, “A prospective study on intravitreal bevacizumab (Avastin®) for neovascular age-related macular degeneration of different durations,” *Acta Ophthalmologica*, vol. 86, no. 5, pp. 482–489, Aug. 2008. DOI: 10.1111/j.1600-0420.2007.01113.x.

[21] K. Ghasemi Falavarjani and Q. D. Nguyen, “Adverse events and complications associated with intravitreal injection of anti-VEGF agents: A review of literature,” *Eye*, vol. 27, no. 7, pp. 787–794, Jul. 2013. DOI: 10.1038/eye.2013.107.

[22] R. P. Finger, M.-T. Puth, M. Schmid, D. Barthelmes, R. H. Guymer, and M. Gillies, “Lifetime outcomes of anti-vascular endothelial growth factor treatment for neovascular age-related macular degeneration,” *JAMA Ophthalmology*, vol. 138, no. 12, pp. 1234–1240, Dec. 1, 2020. DOI: 10.1001/jamaophthalmol.2020.3989.

[23] H. Shahzad, S. Mahmood, S. McGee, *et al.*, “Non-adherence and non-persistence to intravitreal anti-vascular endothelial growth factor (anti-VEGF) therapy: A systematic review and meta-analysis,” *Systematic Reviews*, vol. 12, no. 1, p. 92, Jun. 2, 2023. DOI: 10.1186/s13643-023-02261-x.

[24] F. Ullrich, S. Michels, D. Lehmann, R. S. Pieters, M. Becker, and B. J. Nelson, "Assistive device for efficient intravitreal injections," *Ophthalmic Surgery, Lasers and Imaging Retina*, vol. 47, no. 8, pp. 752–762, Aug. 2016. DOI: 10.3928/23258160-20160808-09.

[25] I. Bekerman, P. Gottlieb, and M. Vaiman, "Variations in eyeball diameters of the healthy adults," *Journal of Ophthalmology*, vol. 2014, pp. 1–5, 2014. DOI: 10.1155/2014/503645.

[26] K.-i. Hosoya and M. Tachikawa, "Inner blood-retinal barrier transporters: Role of retinal drug delivery," *Pharmaceutical Research*, vol. 26, no. 9, pp. 2055–2065, Sep. 1, 2009. DOI: 10.1007/s11095-009-9930-2.

[27] A. Tyagi, P. K. Sharma, and R. Malviya, "Role of blood retinal barrier in drug absorption," *Pharmaceutica Analytica Acta*, vol. 09, Jan. 2018. DOI: 10.4172/2153-2435.1000585.

[28] L. Liu and X. Liu, "Roles of drug transporters in blood-retinal barrier," *Advances in Experimental Medicine and Biology*, vol. 1141, pp. 467–504, Oct. 1, 2019. DOI: 10.1007/978-981-13-7647-4_10.

[29] A. S. Li and S. Fekrat, "The current landscape of anti-VEGF biosimilars," *Retinal Physician*, Sep. 2023.

[30] L. A. Hutton-Smith, E. A. Gaffney, H. M. Byrne, P. K. Maini, D. Schwab, and N. A. Mazer, "A mechanistic model of the intravitreal pharmacokinetics of large molecules and the pharmacodynamic suppression of ocular vascular endothelial growth factor levels by ranibizumab in patients with neovascular age-related macular degeneration," *Molecular Pharmaceutics*, vol. 13, no. 9, pp. 2941–2950, Sep. 6, 2016. DOI: 10.1021/acs.molpharmaceut.5b00849.

[31] S. Zhang, A. Penkova, M. S. Humayun, *et al.*, "In vivo experimental and analytical studies for bevacizumab diffusion coefficient measurement in the rabbit vitreous humor," *Journal of Heat Transfer*, vol. 143, no. 3, Jan. 1, 2021. DOI: 10.1115/1.4049033.

[32] L. M. Hirvonen, G. O. Fruhwirth, N. Srikantha, *et al.*, "Hydrodynamic radii of ranibizumab, aflibercept and bevacizumab measured by time-resolved phosphorescence anisotropy," *Pharmaceutical Research*, vol. 33, no. 8, pp. 2025–2032, Aug. 2016. DOI: 10.1007/s11095-016-1940-2.

[33] H. C. Berg, "Diffusion: Macroscopic theory," in *Random Walks in Biology*, Princeton (NJ): Princeton University Press, 1993, pp. 17–36. DOI: 10.2307/j.ctv7r40w6.7.

[34] T. U. Krohne, Z. Liu, F. G. Holz, and C. H. Meyer, "Intraocular pharmacokinetics of ranibizumab following a single intravitreal injection in humans," *American Journal of Ophthalmology*, vol. 154, no. 4, pp. 682–686, Oct. 2012. DOI: 10.1016/j.ajo.2012.03.047.

[35] T. U. Krohne, N. Eter, F. G. Holz, and C. H. Meyer, "Intraocular pharmacokinetics of bevacizumab after a single intravitreal injection in humans," *American Journal of Ophthalmology*, vol. 146, no. 4, pp. 508–512, Oct. 2008. DOI: 10.1016/j.ajo.2008.05.036.

[36] D. V. Do, W. Rhoades, and Q. D. Nguyen, "Pharmacokinetic study of intravitreal aflibercept in humans with neovascular age-related macular degeneration," *Retina*, vol. 40, no. 4, pp. 643–647, Apr. 2020. DOI: 10.1097/IAE.0000000000002566.

[37] E. M. del Amo, A.-K. Rimpelä, E. Heikkinen, *et al.*, "Pharmacokinetic aspects of retinal drug delivery," *Progress in Retinal and Eye Research*, vol. 57, pp. 134–185, Mar. 2017. DOI: 10.1016/j.preteyeres.2016.12.001.

[38] A. Bonfiglio, R. Repetto, J. H. Siggers, and A. Stocchino, "Investigation of the motion of a viscous fluid in the vitreous cavity induced by eye rotations and implications for drug delivery," *Physics in Medicine and Biology*, vol. 58, no. 6, pp. 1969–1982, Mar. 21, 2013. DOI: 10.1088/0031-9155/58/6/1969.

[39] J. Huang, "Investigations of different methods to promote drug mixing in the eye," Ph.D. dissertation, California Institute of Technology, Dec. 13, 2019. DOI: 10.7907/741T-MN38.

[40] A. Stocchino, R. Repetto, and C. Cafferata, "Eye rotation induced dynamics of a newtonian fluid within the vitreous cavity: The effect of the chamber shape," *Physics in Medicine and Biology*, vol. 52, no. 7, pp. 2021–2034, Apr. 7, 2007. DOI: 10.1088/0031-9155/52/7/016.

[41] A. Stocchino, R. Repetto, and J. H. Siggers, "Mixing processes in the vitreous chamber induced by eye rotations," *Physics in Medicine and Biology*, vol. 55, no. 2, pp. 453–467, Jan. 21, 2010. DOI: 10.1088/0031-9155/55/2/008.

[42] R. K. Balachandran and V. H. Barocas, "Contribution of saccadic motion to intravitreal drug transport: Theoretical analysis," *Pharmaceutical research*, vol. 28, no. 5, pp. 1049–1064, May 2011. DOI: 10.1007/s11095-010-0356-7.

[43] R. K. Balachandran, "Computational modeling of drug transport in the posterior eye," Ph.D. dissertation, University of Minnesota, Jan. 2010.

[44] M. Ferroni, F. De Gaetano, M. G. Cereda, and F. Boschetti, "A drug delivery analysis of large molecules in ocular vitreous chamber: Dependency on saccadic movements after intravitreal injection," *Medical Engineering & Physics*, vol. 82, pp. 49–57, Aug. 1, 2020. DOI: 10.1016/j.medengphy.2020.06.005.

[45] R. Repetto, "An analytical model of the dynamics of the liquefied vitreous induced by saccadic eye movements," *Meccanica*, vol. 41, no. 1, pp. 101–117, Feb. 1, 2006. DOI: 10.1007/s11012-005-0782-5.

[46] S. Vibhute and A. Narasimhan, "Convection-assisted intra-vitreous drug delivery in human eye: An experimental investigation," *Heat Transfer*, vol. 52, no. 7, pp. 4606–4618, May 25, 2023. DOI: 10.1002/htj.22899.

[47] J. Huang and M. Gharib, "Thermal effects on fluid mixing in the eye," *Annals of Biomedical Engineering*, vol. 49, no. 1, pp. 251–261, Jan. 2021. DOI: 10.1007/s10439-020-02534-9.

Chapter 2

VITREOUS MODEL AND REFRACTIVE INDEX MATCHING

2.1 Introduction

This chapter discusses the composition of the human vitreous and presents a procedure for optimizing the working fluid in a vitreous model. Our methodology was designed to identify a working fluid that met the dual constraints of 1) matching the refractive index of the glass eye model to minimize optical distortion and 2) matching the viscosity of a human vitreous to preserve physiologically relevant flow behavior.

2.2 Vitreous Humor

The vitreous humor is a complex, heterogeneous, viscoelastic hydrogel tissue. It is 98-99.7% water and contains hyaluronic acid, glucose, collagen, and ions [1]. Collagen fibers provide the strength and structural integrity to support the gel-state while hyaluronic acid fills the space between the collagen fibers and maintains the pressure that inflates the vitreous chamber [1]. The hyaluronic acid and collagen fibers are not uniformly distributed in the vitreous chamber (Figure 2.1). The central area of the vitreous is more liquid than the vitreous cortex by the retina [2]. For a drug to reach the macula at the back of the eye, it must pass through both regions.

Another complexity of the vitreous humor is that the rheological properties change with age. The vitreous is a gel-like substance at birth and liquefies in heterogeneous patches with age [3]. Liquid vitreous begins to appear after the age of 4, and by the

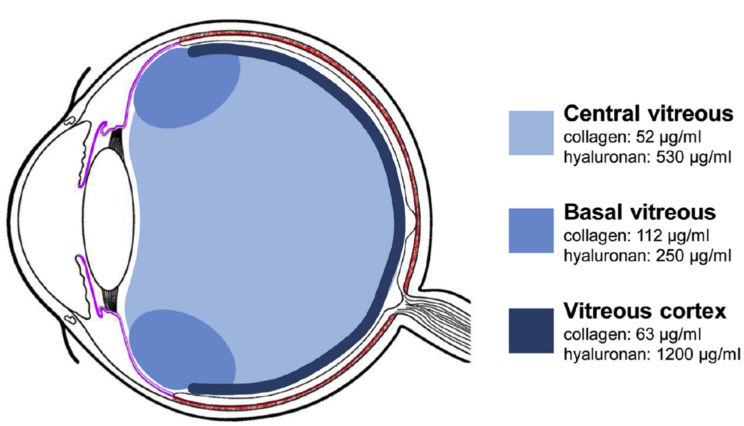

Figure 2.1: Zones of hyaluronic acid concentrations in the vitreous [2].

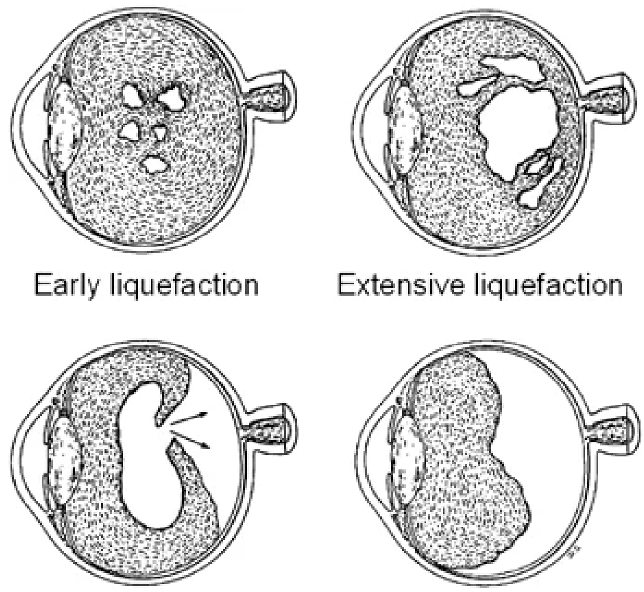

Figure 2.2: Age-related vitreous liquefaction: random patches of liquid appear in the central vitreous and gradually merge (adapted from [1]).

time a person reaches 14–18 years old, approximately 20% of the vitreous volume is liquid. By ages 80–90, more than half of the vitreous has liquefied. This liquefaction process is not uniform across the vitreous cavity. Instead, liquid pockets tend to form in the central vitreous, where they grow and merge (Figure 2.2) [1].

Despite the intricate composition of the vitreous, studies have shown that even in its non-liquefied state, the vitreous is not a tight barrier for diffusion. The mesh size in a bovine vitreous was estimated to be 500nm [4]. As mentioned previously, the hydrodynamic radius of anti-VEGF agents is approximately 4nm [5]. Thus, the stage of liquefaction may not have a significant effect on drug movement [2]. Since regional distributions of liquid and gel components vary between individuals, and drug movement does not appear to be greatly affected by liquefaction, a vitreous model of uniform viscosity is used in this thesis.

The viscosity of the human vitreous ranges from two to four times greater than water [6]. This conclusion is derived from a study by [7]. In the two-component planar heating study by [8], a 20.2% glycerol solution, which matches the viscosity found in the human vitreous, was used. However, our volumetric three-component particle tracking velocimetry experiments necessitate reducing the optical distortion caused by refractive index mismatching. While commercial optical fluids with index of refraction perfectly matched to common transparent materials have been utilized in some studies (e.g. [9]), their high viscosity limits their utility in this work. Given these considerations, we conducted a study to identify a suitable working fluid for our in-vitro vitreous model.

2.3 Vitreous Model

The working fluid of an in-vitro vitreous model is subject to several physical and optical constraints. Firstly, to reduce the distortion and more accurately visualize and measure the flow dynamics, the refractive index of the working fluid must match the eye model. The eye model used in this experiment is nominally made of Pyrex glass but is custom blown, so the refractive index may not match the literature exactly (n=1.474 at 588nm for Pyrex [10], [11]). Secondly, the viscosity of the working fluid must be representative of the human vitreous. Thirdly, a thermal load (ΔT = +3°C) is applied in our two and three-component flow analysis experiments. The refractive index of the working fluid must not change significantly with this temperature change. Lastly, the fluid must be safe to use. A review of the literature (e.g., [10], among others) revealed a promising candidate that largely satisfies the above constraints: sodium iodide.

At 20°C, the viscosity of 55% NaI solution is 2.155 mPas [12], within the range of viscosity of the human vitreous. The National Fire Protection Association rates NaI as 1, 0, 1 for health, flammability, and reactivity, respectively [10]; NaI is stable and poses minimal safety risks. To calculate the refractive index of 55% NaI solution, we look to a study by [13]. In this study, an Abbe refractometer was used to measure the refractive index of NaI solutions for $T = 20 - 35$°C, $c = 55 - 58.5$%, and $\lambda =$ 589.3nm and 632.8nm. The data was fit to the following equation with a standard deviation of 8×10^{-4} and regression coefficient of $R^2 = 0.996$:

$$n_{\mathrm{NaI}}(T, c, \lambda) = 1.252 - \left(2.91 \times 10^{-4}\,{}^{\circ}\mathrm{C}^{-1}\right) T + 0.365c + \frac{5542\,\mathrm{nm}^2}{\lambda^2} \tag{2.1}$$

where:

- n_{NaI} = Refractive index
- T = Temperature (C)
- c = Concentration (%)
- λ = Wavelength (nm).

As described later in Chapter 3: Experimental Setups and Methods, for our experiments, the laser wavelength is 445nm, the ambient temperature is 20°C, and the heater temperature is 23°C. Using Equation 2.1, the refractive index of 55% NaI is 1.4702 and 1.4686 at 20°C and 23°C, respectively. This 0.0016 refractive index decrease is negligible. To prevent the NaI solution from discoloring over time due to I_3^- formation, 0.1% (w/w) sodium thiosulfate ($Na_2S_2O_3$) is added, and Equation 2.1 is inclusive of sodium thiosulfate. Given that NaI appears to meet our constraints, we moved forward with assessing the refractive index matching of different solution concentrations and the eye model.

2.4 Refractive Index Matching Methodology

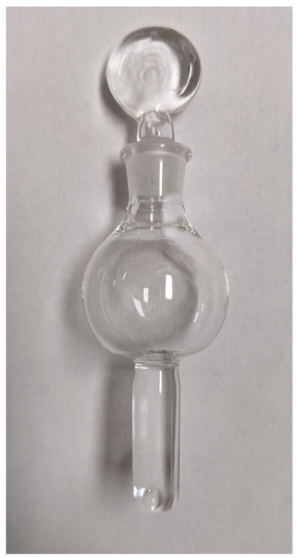

Figure 2.3: Photograph of the eye model used in the refractive index matching experiment.

The eye model used in this refractive index matching experiment was a custom blown glass globe of 25.2mm nominal outside diameter. The eye model has a stem at the base to secure it in place and a hole on the top to fill with fluid, as shown in Figure 2.3. Since the refractive index of the eye model was not known, we analyzed three solutions with physiologically relevant viscosities, 54% NaI solution, 55% NaI solution, and the original 20.2% glycerol solution (Table 2.1). All working solutions were prepared and placed for at least 24 hours at room temperature. To quantify the effect of refractive index mismatch, a homemade grid with 1mm dot spacing and 0.3mm dot diameter was attached to the outside of a 15x15x20cm glass tank, facing inward. The eye model and tank were filled with the working solution, and the eye model was placed in a holder in the tank. A camera (1440 x 1080 pixel resolution, Flir model: BFS-U3-16S2M-CS) aligned directly in front of the eye model captured the image of a back-illuminated calibration grid with and without the eye model in the tank (Figure 2.4). A diagram of the experimental setup is shown in Figure 2.5.

	Dynamic Viscosity (mPas)	Source
Human Vitreous	2-4	[6] derived from [7]
54% NaI solution	2.069	Interpolated from [12]
55% NaI solution	2.155	[12]
Glycerol/Water Mixture (1:5)	1.7	[8]

Table 2.1: The dynamic viscosities of the human vitreous and potential vitreous models, with respective citations.

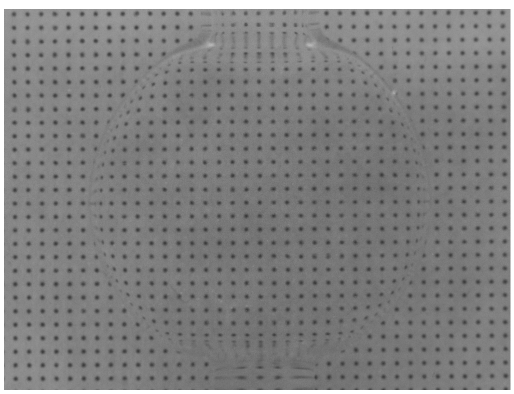

(a)

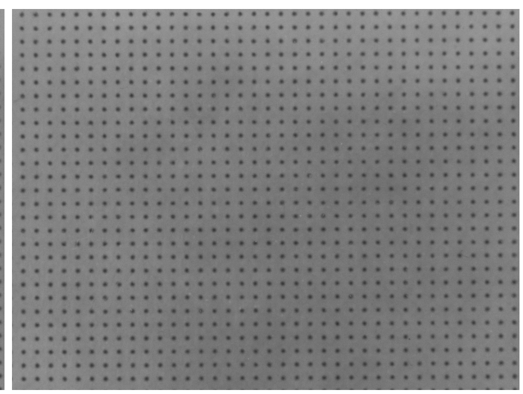

(b)

Figure 2.4: Photographs from the 54% NaI refractive index matching experiment, showing the grid with (a) and without (b) the eye model in the tank.

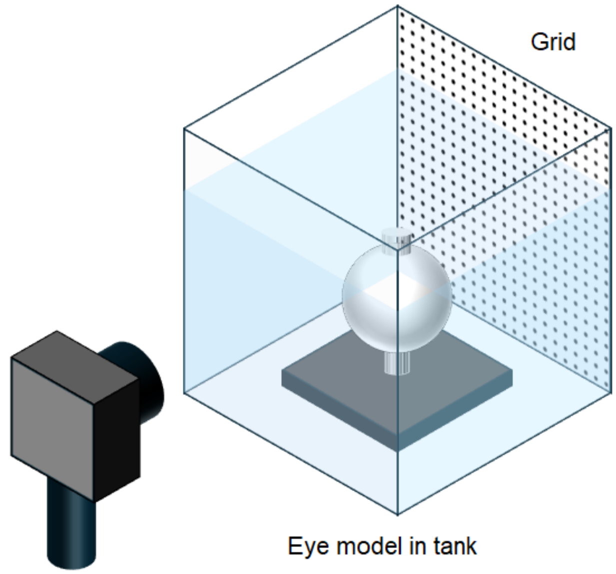

Figure 2.5: Experimental setup: camera on the left faces the eye model, which is placed in a glass tank. Both the eye model and tank are filled with working fluid. The grid is attached to the outside of the glass tank.

PIVlab was used to measure the apparent movement of the grid dots with and without the eye model. Images were imported into PIVlab and analyzed using PIVlab's direct cross-correlation function. The interrogation area, 39 pixels, was carefully chosen to encompass each grid dot. PIV data was split into the undistorted area outside of the eye model on the far left and right sides of the grid, and the area within the glass eye model, which was further divided into 95% radius, 90% radius, and 80% radius. Plots of the grid dot displacement showing the undistorted area and the distorted area subdivision for 54% NaI, 55% NaI, and 20.2% glycerol solutions are shown in Figures 2.6, 2.7, and 2.8, respectively.

The grid dot x-displacement was primarily analyzed, due to the vertical distortion caused by the stem at the base of the eye model and the hole at the top. The grid dot x-displacement data in the undistorted region provided the baseline reference information for perfect index matching; any non-zero value being the combined effect of other optical/imaging artifacts caused by slight vibrations, or movement of components with and without the eye model, and the subpixel accuracy of the software in determining dot displacement. The root mean square for the grid dot x-displacement for the undistorted area was calculated to be 0.39, 0.43 and 0.67 pixels for 54% NaI, 55% NaI, and 20.2% glycerol solutions, respectively. A histogram of the grid dot x-displacement for the undistorted area for all three solutions is shown in Figure 2.9, highlighting the similar baseline displacement values. The RMS values within the eye model are above these thresholds, and represent the additional contribution by the refractive index mismatch of the eye model and working fluid. As expected, the magnitude of the RMS values rises with the increasing size of the region within the eye model due to the larger influence of index mismatch in the region closest to the edges of the eye model. Histograms of the grid dot x-displacement for all three solutions are overlaid for 80% radius in Figure 2.10, 90% radius in Figure 2.11, and 95% radius in Figure 2.12. Comparing RMS values within the eye model for 54% NaI, 55% NaI, and 20.2% glycerol solutions for all radius sizes, shown in Table 2.2, the 54% and 55% NaI solutions have markedly less distortion than the 20.2% glycerol solution. For all radius sizes, the 55% solution has the lowest RMS values, and we note that within 90% radius, the 55% NaI solution has sub-pixel RMS values. Upon comparing results from the different solutions, we concluded that the low RMS values noted here for the 55% NaI solution were sufficient for volumetric three-component particle tracking velocimetry experiments. Further improvement is possible by finer adjustment in the NaI concentration than was considered in this study.

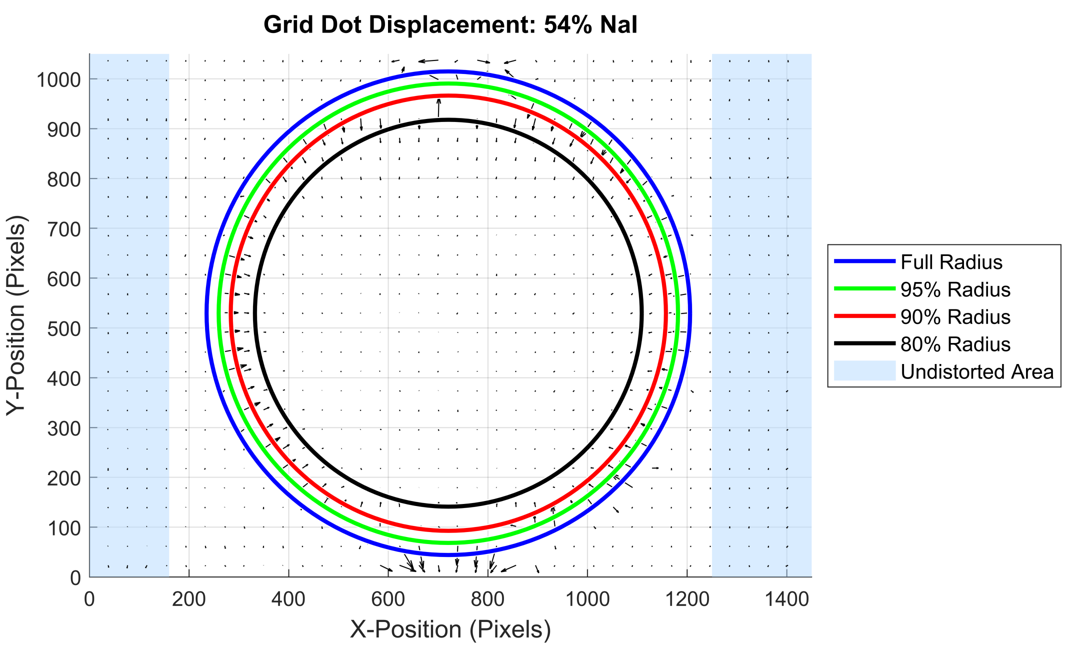

Figure 2.6: Plot of grid dot displacement for 54% NaI solution.

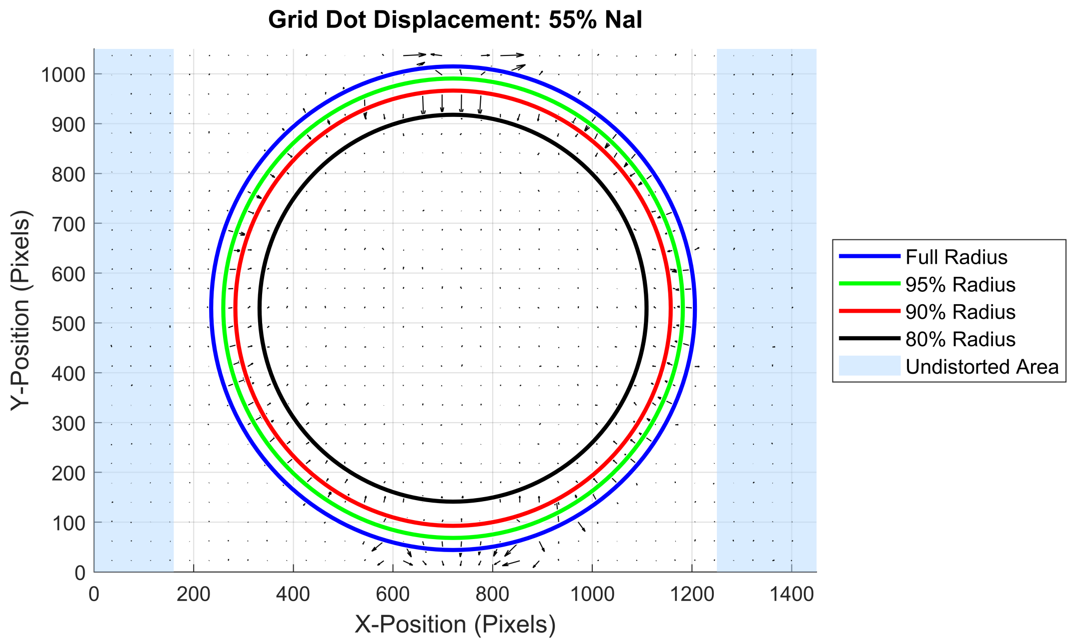

Figure 2.7: Plot of grid dot displacement for 55% NaI solution.

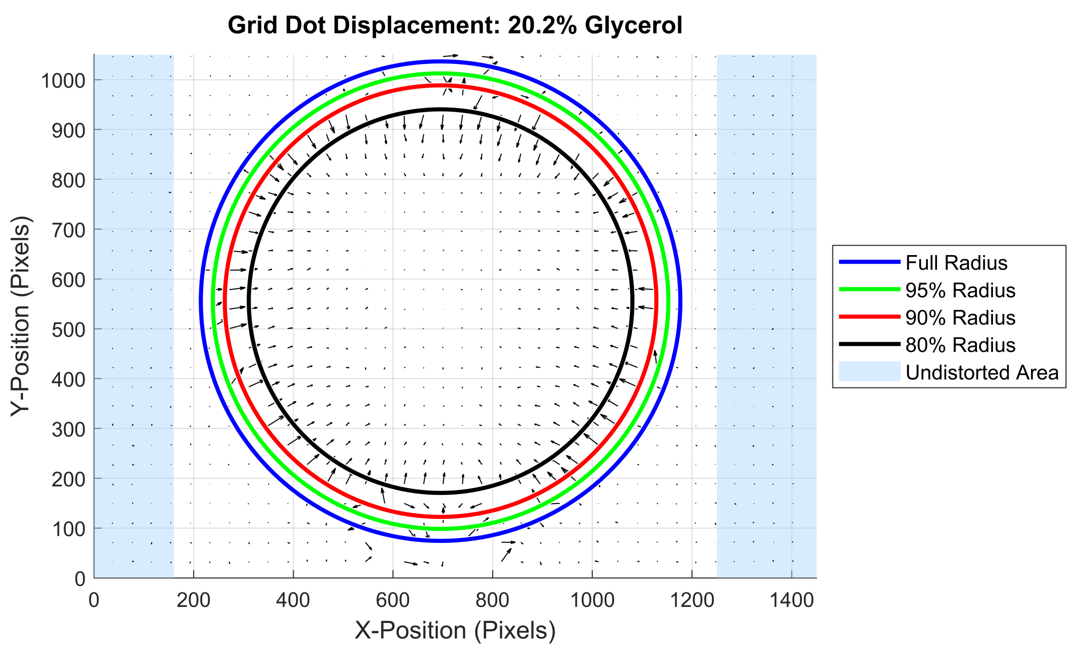

Figure 2.8: Plot of grid dot displacement for 20.2% glycerol solution.

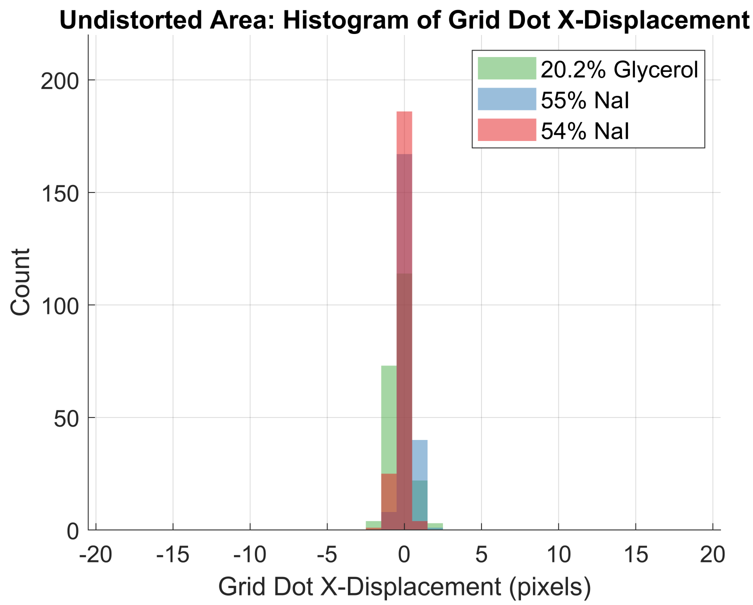

Figure 2.9: Histograms of the grid dot x-displacement for the undistorted area for all solutions are overlaid.

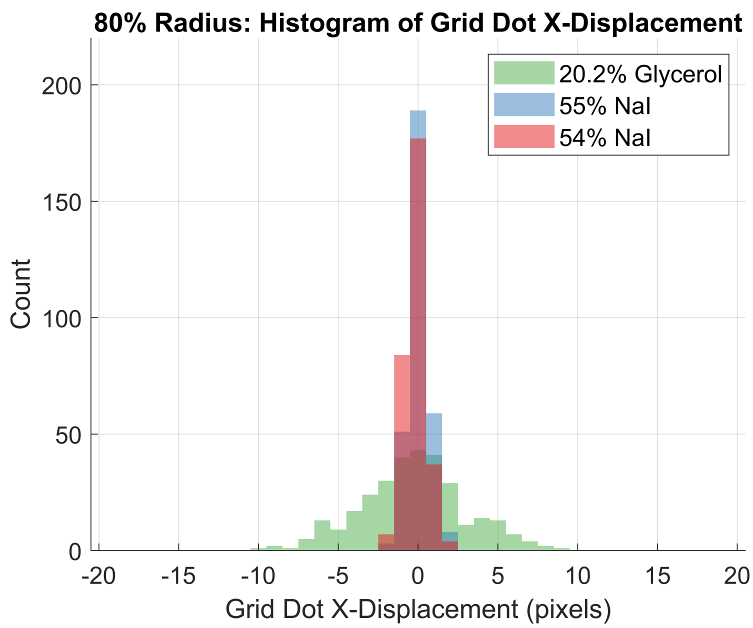

Figure 2.10: Histograms of the grid dot x-displacement for 80% radius for all solutions are overlaid.

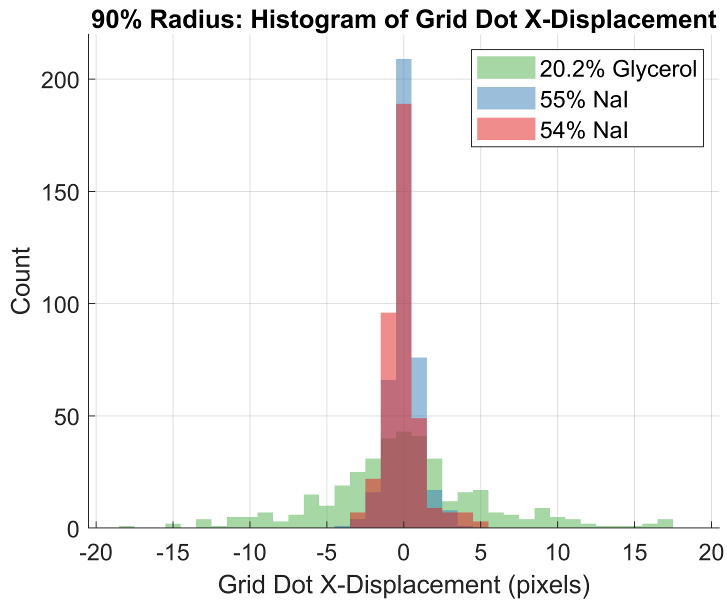

Figure 2.11: Histograms of the grid dot x-displacement for 90% radius for all solutions are overlaid.

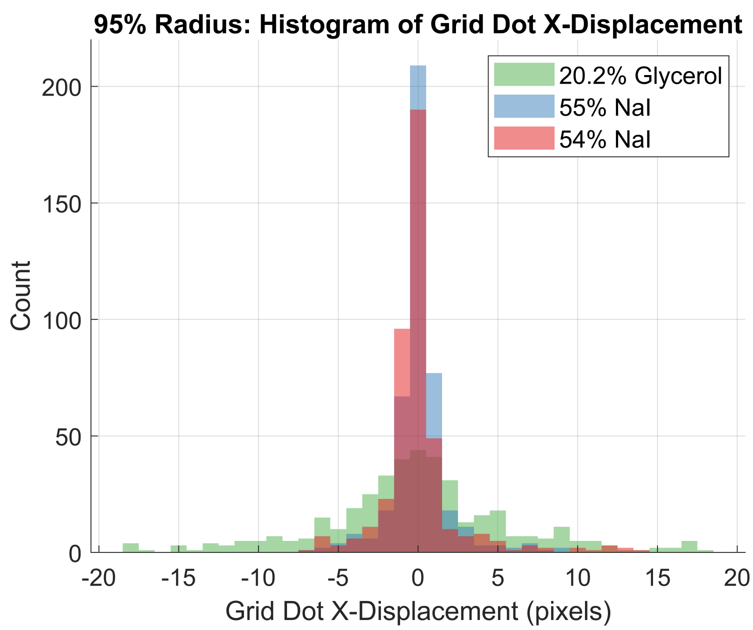

Figure 2.12: Histograms of the grid dot x-displacement for 95% radius for all solutions are overlaid.

Working Fluid	Undistorted	80% radius	90% radius	95% radius
54% NaI	0.39	0.70	1.41	2.04
55% NaI	0.43	0.63	0.96	1.74
20.2% Glycerol	0.67	3.32	5.42	6.05

Table 2.2: Root mean square values for grid dot x-displacement for the undistorted area and different radius sizes for 54% NaI, 55% NaI, and 20.2% glycerol solutions.

2.5 Conclusion

This chapter demonstrates a refractive index matching technique that can be used to improve flow visualization and measurement experiments. Using a simple grid and PIVlab, we were able to quickly and systematically find a solution, 55% NaI, that sufficiently matched the refractive index of the eye model, as well as the unique constraints of our experiments. This refractive index matching technique can be applied more broadly and proves especially useful when the exact refractive index of the model or the solution is not known. If closer index matching is needed, the process described here could be repeated with different solution concentrations until the desired refractive index matching is achieved. Furthermore, the grid dot displacement values from the refractive index matching analysis, which quantify the optical distortion, could potentially be used to correct the velocity values calculated from flow measurement experiments. This would allow for more accurate velocity calculations, particularly near the edges of the eye model, which would be valuable for assessing wall shear stress and other related parameters.

In the subsequent chapters, we used this vitreous model, 55% NaI solution, to perform both planar and volumetric flow measurement and visualization experiments with reduced optical distortion.

Chapter References

[1] M. M. Le Goff and P. N. Bishop, "Adult vitreous structure and postnatal changes," *Eye*, vol. 22, no. 10, pp. 1214–1222, Oct. 2008. DOI: 10.1038/eye.2008.21.

[2] E. M. del Amo, A.-K. Rimpelä, E. Heikkinen, *et al.*, "Pharmacokinetic aspects of retinal drug delivery," *Progress in Retinal and Eye Research*, vol. 57, pp. 134–185, Mar. 2017. DOI: 10.1016/j.preteyeres.2016.12.001.

[3] T. Root, "OphthoBook." CreateSpace Independent Publishing Platform, Jul. 20, 2009.

[4] Q. Xu, N. J. Boylan, J. S. Suk, *et al.*, "Nanoparticle diffusion in, and microrheology of, the bovine vitreous ex vivo," *Journal of Controlled Release*, vol. 167, no. 1, pp. 76–84, Apr. 2013. DOI: 10.1016/j.jconrel.2013.01.018.

[5] L. M. Hirvonen, G. O. Fruhwirth, N. Srikantha, *et al.*, "Hydrodynamic radii of ranibizumab, aflibercept and bevacizumab measured by time-resolved phosphorescence anisotropy," *Pharmaceutical Research*, vol. 33, no. 8, pp. 2025–2032, Aug. 2016. DOI: 10.1007/s11095-016-1940-2.

[6] K. R. Murthy, R. Goel, Y. Subbannayya, *et al.*, "Proteomic analysis of human vitreous humor," *Clinical Proteomics*, vol. 11, no. 1, p. 29, Dec. 2014. DOI: 10.1186/1559-0275-11-29.

[7] J. C. Locke and W. R. Morton, "Further studies of the viscosity of aspirated human vitreous fluid: With special reference to its use in retinal detachment surgery," *Transactions of the American Ophthalmological Society*, vol. 63, pp. 129–145, 1965.

[8] J. Huang and M. Gharib, "Thermal effects on fluid mixing in the eye," *Annals of Biomedical Engineering*, vol. 49, no. 1, pp. 251–261, Jan. 2021. DOI: 10.1007/s10439-020-02534-9.

[9] S. Rayepalli, R. Gupta, C. Lum, A. Majid, and M. Koochesfahani, "The impact of stent strut porosity on reducing flow in cerebral aneurysms," *Journal of Neuroimaging*, vol. 23, no. 4, pp. 495–501, Oct. 2013. DOI: 10.1111/jon.12044.

[10] P. Miller, K. Danielson, G. Moody, A. Slifka, E. Drexler, and J. Hertzberg, "Matching index of refraction using a diethyl phthalate/ethanol solution for in vitro cardiovascular models," *Experiments in Fluids*, vol. 41, no. 3, pp. 375–381, Aug. 24, 2006. DOI: 10.1007/s00348-006-0146-5.

[11] Corning, Inc., "PYREX® and Corning® Glass and Reusable Plastic Product Selection Guide: CLS-GL-001."

[12] I. D. Zaytsev and G. G. Aseyev, "Properties of Aqueous Solutions of Electrolytes." Taylor & Francis, 1992.

[13] T. L. Narrow, M. Yoda, and S. I. Abdel-Khalik, "A simple model for the refractive index of sodium iodide aqueous solutions," *Experiments in Fluids*, vol. 28, no. 3, pp. 282–283, Mar. 6, 2000. DOI: 10.1007/s003480050389.

Chapter 3

EXPERIMENTAL SETUPS AND METHODS

3.1 Introduction

The experimental setups in this thesis were designed for both planar two-component and volumetric three-component flow measurement and visualization in an in-vitro vitreous model. The planar two-component experiments utilized particle image velocimetry (PIV) to measure the flow field on a thin plane at the center of the eye model. The volumetric three-component experiments employed Tomographic Aperture-encoded Particle Tracking Velocimetry (TAPTV) to capture the flow field throughout the eye model. This chapter details the imaging techniques, software, and materials used, along with their preparation.

3.2 Materials

Eye Model

The vitreous chamber is a slightly deformed sphere [1], [2], and the eye model used for flow measurement and visualization experiments, shown in Figure 3.1, is a custom-blown Pyrex globe with nominal outside diameter of 25mm. The eye model has a hole at the top to fill with 55% NaI solution mixed with neutrally buoyant particles (model: Cospheric LLC: Conductive Silver-Coated PMMA Microparticles 1.7g/cc 38-45um). To ensure the particles are neutrally buoyant, the particles are mixed with the 55% NaI solution in a beaker and left untouched for 20 minutes.

Figure 3.1: Eye model used for planar and volumetric flow measurement and visualization experiments.

After 20 minutes, the solution is pipetted from the center of the beaker into the eye model. Greater particle density is used for planar experiments compared to volumetric experiments.

Heat Source

The experiments in this thesis focus on heating from below the eye model, against gravity. In a human subject, heating from below would be equivalent to applying a heat source to the eye while laying face-down. In the two-dimensional PIV study by [3], the strongest fluid mixing was observed when heating was applied against gravity, either in the inferior position for an upright person or in a face-down orientation (Figure 3.2 (a)). Since the face-down position reached the highest absolute circulation value (Figure 3.2 (b)), we chose to focus this thesis on face-down heating, with the bottom of the eye model representing the front of the eye and the top of the eye model representing the macula, as illustrated in Figure 3.3 (b).

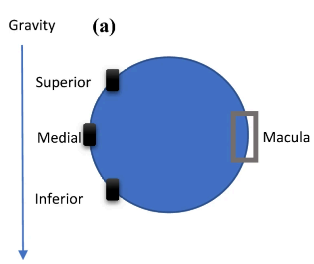

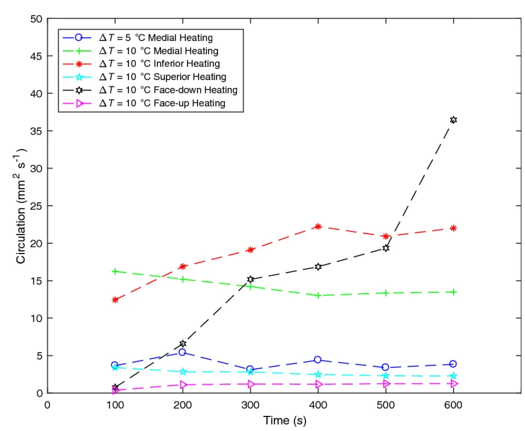

(a) (b)

Figure 3.2: Figures from [3]. (a) Select heating positions, where the heater location is marked in black, and the position of the target tissue is marked by a hollow gray square. Left and right images show upright and face-down heating positions, respectively. (b) Plot of the absolute value of circulation, calculated from planar PIV data for each heating case.

Our heat source, shown in Figure 3.3 (a), was composed of a custom 3D-printed part, small Peltier thermoelectric heater (model: TEC1-12706), and two thermal pads. The 3D-printed part holds the eye model and heater in place and provides a black background for flow imaging. A base thermal pad (model: Kritical Thermal Pads – 20 W/mk conductivity – 3.0mm thickness) was cut to size and applied directly

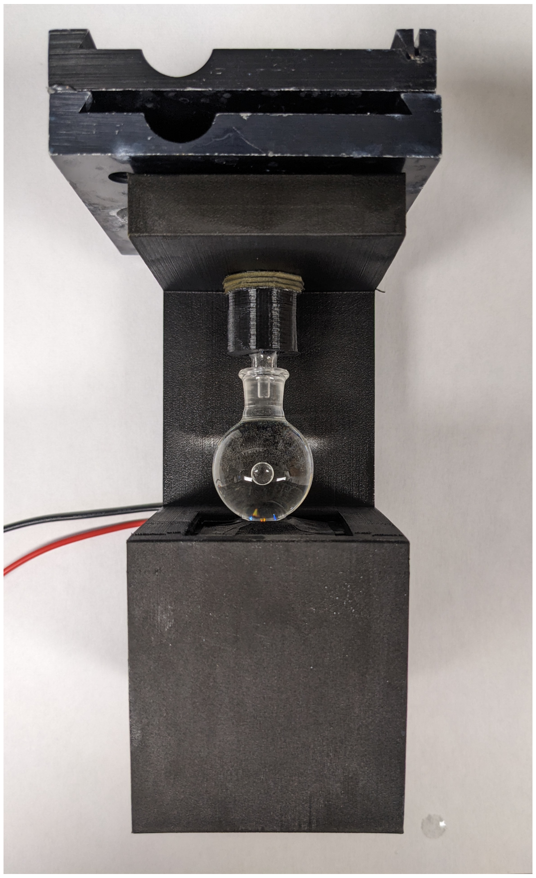

(a)

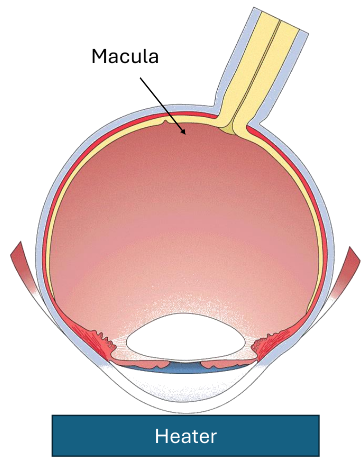

(b)

Figure 3.3: "Face-down" heating configuration. (a) Photograph of the eye model on top of the heat source, consisting of the 3D-printed part, heater, and thermal pads. (b) Diagram of the face-down heating orientation.

to the Peltier heater. On top of this thermal pad, a thin black graphite thermal pad (model: ADWITS graphite thermal pad – 0.07mm thickness) was applied. The black thermal pad was used to reduce glare from the laser. The Peltier heater was connected to a power source which was set to 2.3 volts, equivalent to a 3°C thermal load.

A 3°C thermal load was chosen given safety and thermal conductivity considerations. There are two FDA-approved ocular heating devices, Lipiflow and Tearcare, designed for the treatment of dry eye. For Lipiflow, a temperature of 42.5°C is applied directly to the inner eyelid, while Tearcare delivers 45°C to the outer surface of the eyelid [4]. Heat exceeding 45°C at the outer eyelid can begin to present safety risks [5]–[9]. The human body is 37°C, so a 3°C thermal load is below both the safety threshold and these FDA-approved ocular devices.

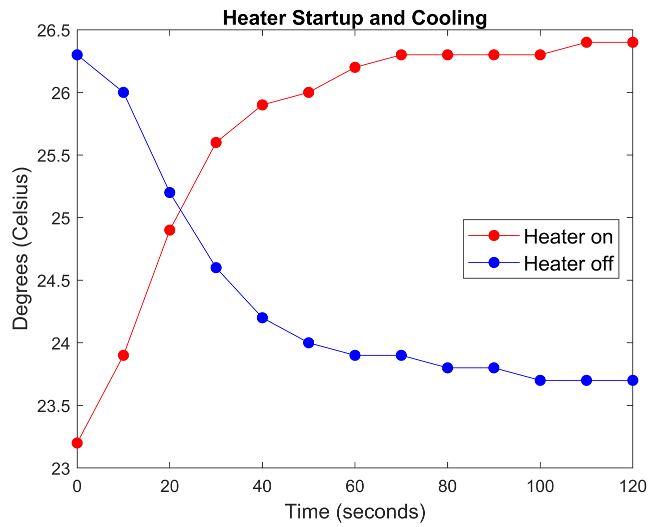

Figure 3.4: Plot showing the temperature versus time of the heat source when the power source is turned on and off.

Another consideration, 55% NaI solution is less thermally conductive (k = 0.464 [10]) compared to ocular tissue (k = 0.58 and 0.594 for cornea and vitreous humor, respectively [11]), which would allow the liquid in our eye model to heat up more easily than a human eye. This indicates that for real eye applications, a higher temperature difference is likely to be preferred. The 3°C thermal load being well-below the safety threshold offers more flexibility for applications on human eyes.

To get the temperature profile of our heat source, a thermocouple was attached to the top of the outer thermal pad. The heat source was submerged, and the power source was turned on. The temperature was recorded every 10 seconds for 2 minutes. The power source was then turned off, and the recording process was repeated. The profile for the temperature of the heat source over time is shown in Figure 3.4. When turned on, the heater reaches 80% of its final temperature in approximately 30 seconds. The heater cools approximately 70% in 30 seconds. The constant 2.3V power source ensures there are minimal temperature fluctuations once the maximum temperature is achieved.

3.3 Volumetric Three-Component Imaging Technique

For three-dimensional flow visualization and measurement, volumetric Tomographic Aperture-encoded Particle Tracking Velocimetry (TAPTV) experiments are performed.

TAPTV is a three-dimensional particle tracking technique designed for high-resolution flow measurements. It integrates the principles of tomographic

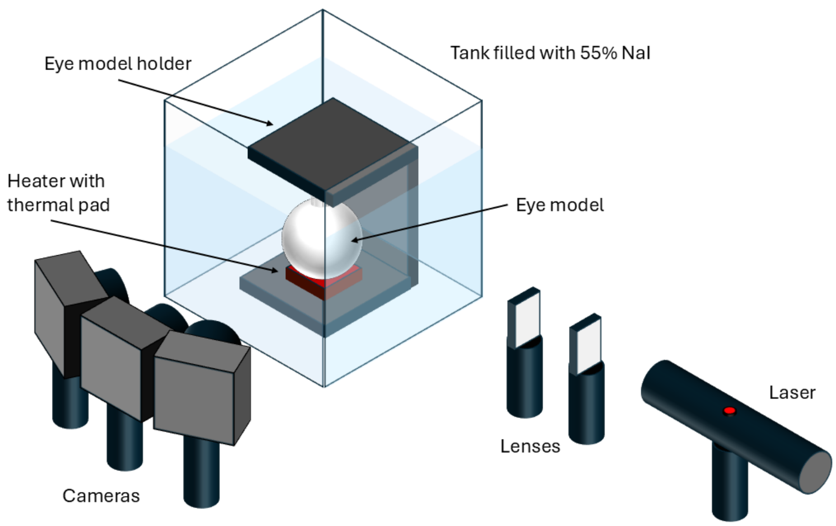

Figure 3.5: Diagram of the volumetric flow visualization and measurement experimental setup, with three cameras, heat source, two convex lenses, tank, and laser.

imaging, aperture encoding, and particle tracking velocimetry to reconstruct the full three-dimensional motion of particles suspended in a fluid. Unlike conventional PIV, which cross-correlates between particle patterns within interrogation windows, or standard PTV, which suffers from occlusions at high seeding densities, TAPTV utilizes multiple camera views and optical encoding to extract depth information. Once a particle is identified and matched across multiple cameras, it is tracked across successive frames.

The three-dimensional experimental setup described here was custom-made. Images taken were adapted for use with the commercially available software, "Insight V3V 4G Software for Volumetric 3-Component Velocimetry Flow Measurement Systems."

Experimental Setup

The experimental setup captures synchronized images of illuminated tracer particles from different angles, allowing for the reconstruction of a volumetric measurement domain. The three-component experimental setup, shown in Figures 3.5 and 3.6, consisted of a laser, heat source, eye model, three cameras, two cylindrical lenses, and a 15x15x20cm tank filled with 55% NaI solution. The heat source was placed at the center of the tank, with the eye model on top of the thermal pad. A 1W 445nm

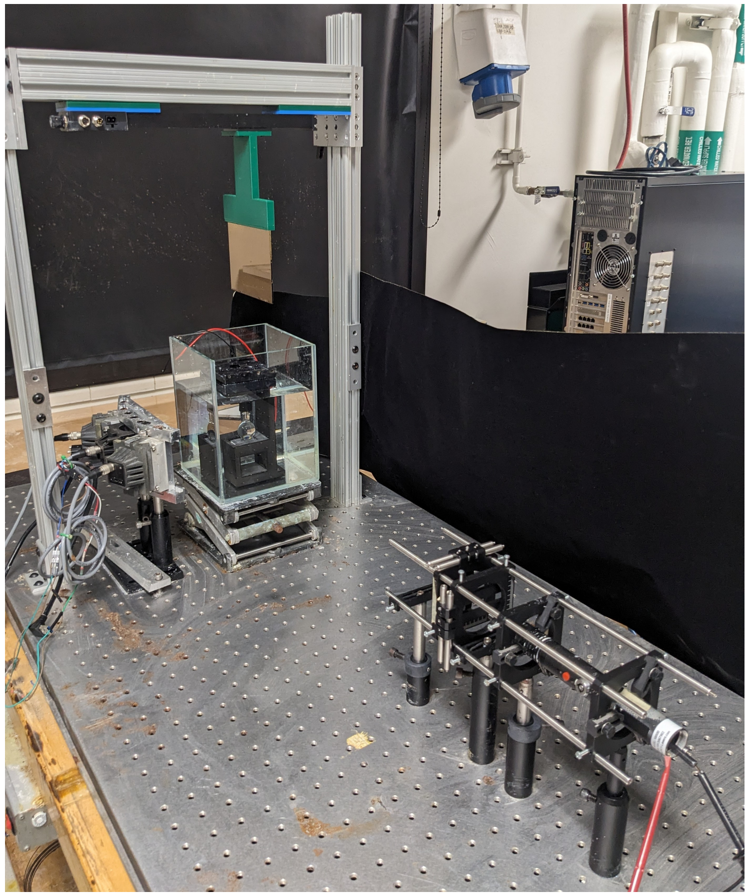

Figure 3.6: Photograph of the actual volumetric flow visualization and measurement experimental setup, with three cameras, heat source, two convex lenses, tank, and laser.

blue CW laser (model: SKY 1912067902) was used for illumination. The laser is connected to a power source set to 4.9V. This ensures the brightness of the laser is consistent over the course of the experiment and between experimental runs. The first cylindrical lens was used to spread the laser beam vertically into a thin sheet, and the second cylindrical lens expands the laser sheet into a block of laser light that illuminates the entire eye model, allowing the cameras to capture the tracer particles throughout the volumetric flow field.

Three compact cameras are set up in front of the tank; one directly in front of the eye model and two angled 20° on either side of the middle camera. The cameras (1440x1080 pixel resolution, camera model: Flir BFS-U3-16S2M-CS) were soldered together, and the Spinnaker SDK software was used to trigger all three cameras simultaneously. Example experiment images are shown in Figure 3.7. During each visualization session, a total of 60,000 images were taken by each

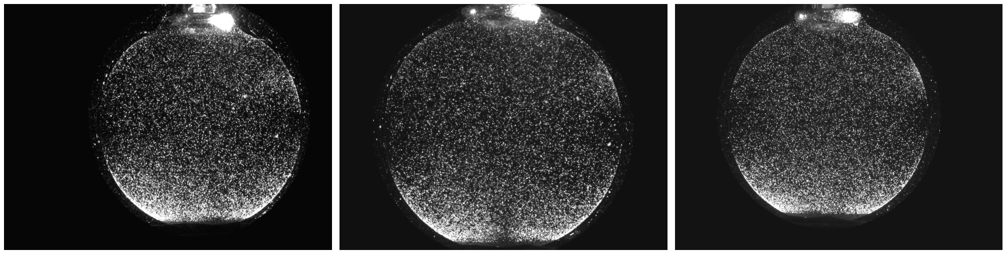

Figure 3.7: Example photographs from a three-component volumetric PTV experiment. Images from left to right are taken by the left, center, and right cameras, respectively. Photographs here are enhanced using ImageJ.

camera, for a total of 180,000 images. Each experiment was 10 minutes long, and the camera frame rate was set to 100 FPS.

Calibration Setup

The calibration process in TAPTV serves as a crucial reference for establishing an accurate mapping between the 2D camera images and the real-world 3D coordinate system.

The calibration setup is shown in Figure 3.8. The calibration target, shown in Figure 3.9, features grid points spaced 2mm apart, each with a diameter of 0.3mm. Three missing grid points serve as a fiducial mark. The calibration target was printed on soda lime glass and purchased from HTA Photomask. A custom 3D-printed part attached the calibration target to a traverse (model: Zaber X-LSM200A-E03, a motorized linear stage with an integrated encoder, controller, and 60µm accuracy). The calibration target was lowered into the tank filled with 55% NaI solution and positioned towards the back of the tank. To illuminate the grid pattern on the calibration target, a light tracing pad (model: LitEnergy A4 LED Copy Board Light Tracing Box) was placed behind the tank. The traverse was marched forward 2mm at a time, with the three cameras capturing the image of the calibration target at each step, until the traverse passed through the entirety of the measurement volume.

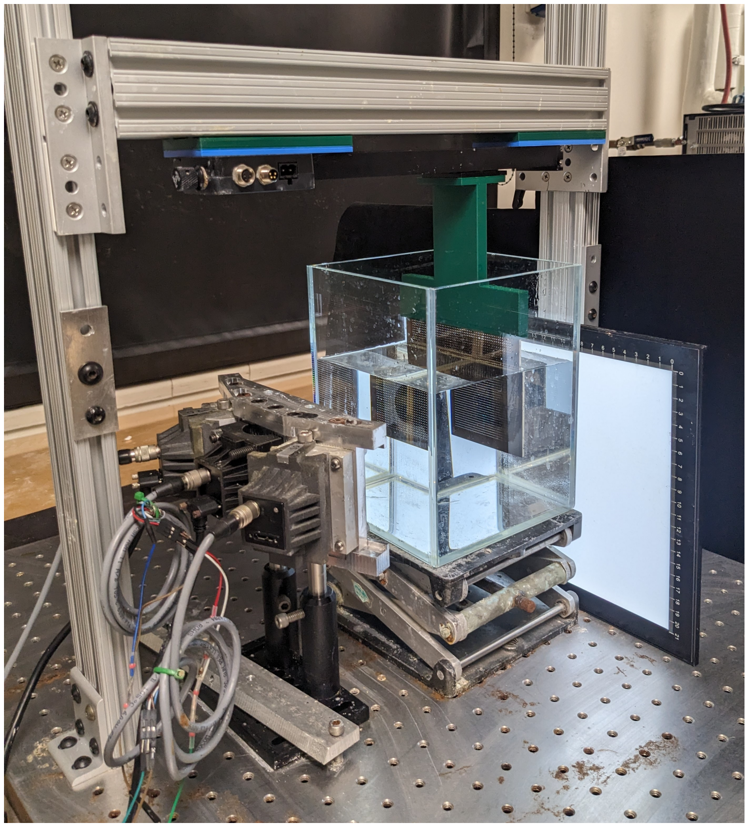

Figure 3.8: Photograph of the actual calibration setup, with three cameras, tank, traverse, calibration target, and backlight.

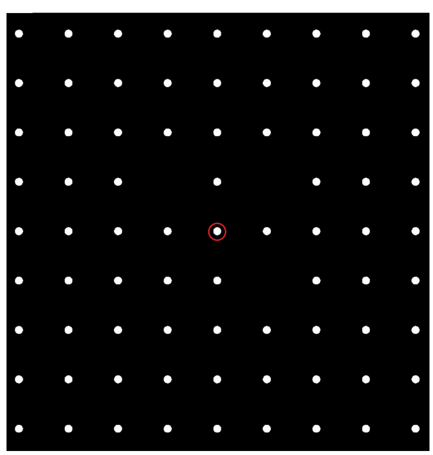

Figure 3.9: Calibration target with center of fiducial mark circled in red.

Analyzing the Calibration Images

A custom MATLAB script renamed images from the calibration setup to match the V3V software's required naming convention. The renamed images were then imported into the V3V software and assigned "Tiff tags" using the Image Tools tab.

Once the calibration images were loaded and tagged, they underwent pre-processing to aid in grid point and fiducial mark identification. The "Tiff tags" and settings for pre-processing can be found in Appendix: Experimental Setup.

After pre-processing, calibration processing begins with particle identification to detect and analyze fiducial markers. The intensity threshold is set to distinguish calibration particle images from background noise. Pixels with intensity values above this threshold are grouped into support sets, which are contiguous regions of pixels likely to belong to the same particle. Each support set is expected to contain only one calibration particle image. Local mean subtraction is applied to remove non-uniform illumination effects and enhance contrast for improved detection. Once the support sets are identified, the algorithm determines the size and location of the calibration points using gaussian intensity profile fitting.

Using these detected markers, a calibration mapping function is computed for each camera, correcting for lens distortions, misalignments, and perspective errors. A mapping function relates three-dimensional (world) coordinates to two-dimensional (image) coordinates. We found the calibration process achieved the best results when the mapping function was set to automatic. For an automatic selection of mapping function polynomial order, Insight V3V 4G software will compute second, third, and fourth order polynomials and choose that which resulted in the lowest error. The full processing settings that we used for the calibration are in Appendix: Experimental Setup.

To ensure the accuracy of the calibration prior to conducting three-component velocity measurement experiments, we verified the calibration results. We examined the calibration plots for obvious errors; for example, the nominal magnification should smoothly increase as the calibration target advances toward the cameras. Additionally, the grid points identified at each z-position were cross-verified by inspecting corresponding raw images.

Over the course of running the three-component experiments, a traverse malfunctioned. The issue was not immediately apparent, as the physical calibration process appeared to be successful, and the calibration plots did not reveal any obvious anomalies. To further validate the calibration, we performed both pre-processing and processing steps using the set of calibration images. These same images were then imported as experiment image sets to confirm that the software was correctly mapping the grid points within the measurement volume. Through this approach, we discovered that the traverse was not moving exactly 2mm per step as programmed, but instead deviated slightly above or below the target displacement. This discrepancy introduced significant errors in the experiment image processing.

Once the calibration images were processed and verified, the experiment images were analyzed.

Analyzing the Experiment Images

The experiment images were copied, to allow for A/B image pairing. Like the calibration images, a custom MATLAB script renamed the experiment images according to the V3V software's naming convention. The renamed experiment images were then loaded simultaneously into the software using the Image Tools tab, and "Tiff tags" were assigned to the images.

After the images were loaded and tagged, a mask was carefully drawn around the edge of the eye model for all three camera images. Pre-processing followed, to remove noise and improve the accuracy of particle detection and tracking. A minimum intensity image was generated and subtracted from each raw image to improve the signal-to-noise ratio. A gaussian image filter was used to improve particle detection. The "Tiff tags" and full pre-processing settings are shown in order in Appendix: Experimental Setup.

The V3V software has three core processors for the experiment images: particle identification, particle matching, and particle tracking. Particle identification is the first step in the processing pipeline and is responsible for identifying (i.e., locates, sizes, and determines intensity of) particle images.

After particle identification, the particle matching processor takes the lists of two-dimensional particle images. First, it attempts to match each particle image by using each camera's calibration, drawing epipolar lines in each camera, and locating particle images that are within a user-set tolerance of pixels of each line. If a match is successful, it reconstructs the particle with three-dimensional coordinates.

Once the particles are reconstructed in three-dimensional space, the particle tracking processor tracks their motion across successive frames. The tracking algorithm that yielded the best results for our experiment images was the relaxation method [12]. Additionally, outlier detection filters, like the Universal Median Filter and Global Range Filter, were used to remove invalid vectors.

Since the tracer particles were randomly distributed throughout the eye model, particle vectors were also randomly distributed. Interpolation was required to map velocity data onto a Cartesian grid. This process used gaussian weighting, where vectors closer to the center of a grid node contribute more significantly to the interpolation than those farther away. The weighting is determined by a gaussian kernel. Furthermore, the vector interpolation processor smooths the resulting vector fields by incorporating contributions from neighboring vectors. The custom settings for processing our three-component experiments can be found in Appendix: Experimental Setup.

The grid velocity fields for all frames were exported from the software. A final post-processing step was then applied, consisting of ensemble averaging and further outlier correction. The grid velocity data was averaged over 100-frame intervals, yielding one time-averaged grid velocity field per second, resulting in a total of 600 velocity fields per 10-minute experiment. Outlier correction was performed using a moving median filter, wherein outliers are identified based on deviations from the local median computed within a sliding spatial window. Outliers were replaced using linear interpolation, which estimates missing or extreme values based on neighboring data points.

The number of particles in the eye model that were successfully tracked between frames varied but was typically in the range of 1500-2500 particles. This is equivalent to a spatial density of approximately 0.2 vectors per cubic millimeter. These vectors were then interpolated onto a volumetric grid with 1mm spacing for a total of about 16000 gridded vectors.

3.4 Planar Two-Component Imaging Technique

Experimental Setup

For planar two-component experiments, the volumetric three-component experimental setup was adjusted. The planar experimental setup, shown in Figure 3.10, consisted of a camera, cylindrical lens, laser, heat source, eye model, and tank filled with 55% NaI solution. The single cylindrical lens was used to spread the laser beam vertically into a thin sheet. The sheet of light was carefully aligned through the center of the eye model, allowing for a camera to capture the planar

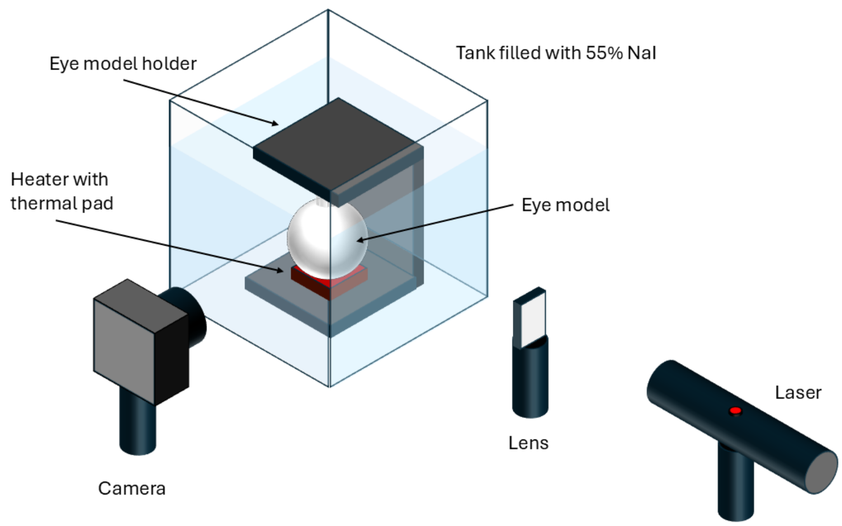

Figure 3.10: Two-dimensional flow measurement and visualization experimental setup, including eye model, heat source, tank, camera, lens, and laser.

flow profile. The flow images were captured by the center camera in the volumetric experimental setup. The camera was controlled using the free Spinnaker SDK software. During each visualization session, a total of 6,000 images were taken. Each experiment was 10 minutes long, and the camera frame rate was set to 10 FPS.

Obtaining the Velocity Field

For quantitative measurements, flow images were cross-correlated using PIVlab [13]. The images were imported into PIVlab, and the "region of interest" was defined as a square encompassing the eye model. A mask was then carefully drawn along the edge of the eye model, so that the software analyzed only the area within the eye model (Figure 3.11). Images were analyzed using the direct Fourier transform correlation with multiple passes and deforming windows. With this algorithm, the first pass uses larger interrogation areas to ensure reliable displacement calculations with a high signal-to-noise ratio. However, since larger interrogation areas result in low vector resolution, limiting the number of velocity vectors per frame, the interrogation window in the second pass is reduced, in order to improve resolution [14]. The PIVlab settings used in this thesis are available in Appendix: Experimental Setup.

After the vectors are calculated, a calibration is completed to convert the units from

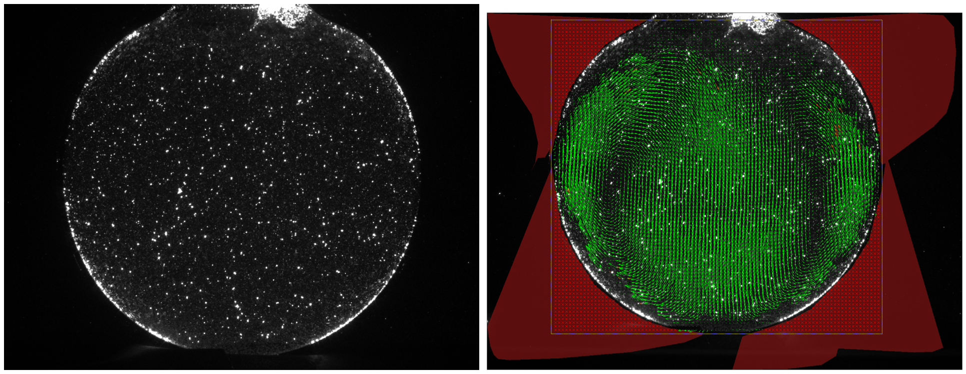

(a) (b)

Figure 3.11: Example image from a planar flow experiment. (a) Raw photograph. (b) Same image processed in PIVlab. The white square indicates the region of interest where the velocity field is analyzed. The red mask excludes areas outside the eye model from analysis. Orange vectors represent interpolated values; green vectors represent valid measurements.

pixels/seconds to meters/second. The reference length, the diameter of the eye model, is drawn on the flow image and set to 25mm. A standard deviation filter threshold is set to 8 to remove outliers after processing. The spatial density for the PIVlab data is approximately 3 grid points per millimeter.

3.5 Particle Pathline Analysis

Particle pathlines track the trajectory of individual fluid particles over time. Particle pathlines provided valuable insight into how a heating condition may affect an injection reaching the target area.

Using the planar or volumetric velocity field data, the Lagrangian path of a fluid element can be tracked to generate a pathline visualization in MATLAB. Forward Euler integration is used. The process begins by defining the initial positions of selected particles and plotting them. Then, at each time step, the corresponding velocity field data is referenced to calculate and plot the subsequent positions. This procedure is repeated over a defined time period, generating the pathline corresponding to each particle's initial position. Table 3.1 outlines the procedure for pathline progression.

x progression	y progression	point coordinate
$x_0 = x_0$	$y_0 = y_0$	(x_0, y_0)
$x_1 = x_0 + u(x_0, t_0) \cdot dt$	$y_1 = y_0 + v(y_0, t_0) \cdot dt$	(x_1, y_1)
$x_2 = x_1 + u(x_1, t_1) \cdot dt$	$y_2 = y_1 + v(y_1, t_1) \cdot dt$	(x_2, y_2)

Table 3.1: Progression of particle positions using two-component velocity data.

Qualitative Two-Dimensional Pathlines

For qualitative flow mapping, planar experiment images were loaded into the open-source, Java-based image processing software, ImageJ [15]. The plugin "Grouped ZProjector" was used to overlay images, with the projection method set to maximum intensity. The flow images were segmented into groups of 10 consecutive frames, corresponding to a 1-second time interval. Z-projection allows for a visualization of short flow pathlines, which is especially helpful in video format to observe changes over time. Key characteristics of the flow field can be seen, such as vortices and point sources.

Chapter References

[1] S. E. Skalicky, "The vitreous," in *Ocular and Visual Physiology: Clinical Application*, Singapore: Springer, 2016, pp. 99–104. DOI: 10.1007/978-981-287-846-5_7.

[2] J. Meskauskas, R. Repetto, and J. H. Siggers, "Shape change of the vitreous chamber influences retinal detachment and reattachment processes: Is mechanical stress during eye rotations a factor?" *Investigative Ophthalmology & Visual Science*, vol. 53, no. 10, pp. 6271–6281, Sep. 2012. DOI: 10.1167/iovs.11-9390.

[3] J. Huang and M. Gharib, "Thermal effects on fluid mixing in the eye," *Annals of Biomedical Engineering*, vol. 49, no. 1, pp. 251–261, Jan. 2021. DOI: 10.1007/s10439-020-02534-9.

[4] M. W. Beining, M. S. Magnø, E. Moschowits, *et al.*, "In-office thermal systems for the treatment of dry eye disease," *Survey of Ophthalmology*, vol. 67, no. 5, pp. 1405–1418, Sep. 1, 2022. DOI: 10.1016/j.survophthal.2022.02.007.

[5] C. J. Kenrick and S. S. Alloo, "The limitation of applying heat to the external lid surface: A case of recalcitrant meibomian gland dysfunction," *Case Reports in Ophthalmology*, vol. 8, no. 1, pp. 7–12, Jan. 16, 2017. DOI: 10.1159/000455087.

[6] D. Borchman, "The optimum temperature for the heat therapy for meibomian gland dysfunction," *The Ocular Surface*, vol. 17, no. 2, pp. 360–364, Apr. 2019. DOI: 10.1016/j.jtos.2019.02.005.

[7] C. A. Blackie, C. W. McMonnies, and D. R. Korb, "Warm compresses and the risks of elevated corneal temperature with massage," *Cornea*, vol. 32, no. 7, e146–149, Jul. 2013. DOI: 10.1097/ICO.0b013e318292a7b7.

[8] B. Bzovey and W. Ngo, "Eyelid warming devices: Safety, efficacy, and place in therapy," *Clinical Optometry*, vol. 14, pp. 133–147, Aug. 5, 2022. DOI: 10.2147/OPTO.S350186.

[9] D.-H. Wang, H. Guo, W. Xu, and X.-Q. Liu, "Efficacy and safety of the disposable eyelid warming masks in the treatment of dry eye disease due to meibomian gland dysfunction," *BMC Ophthalmology*, vol. 24, no. 1, p. 376, Aug. 26, 2024. DOI: 10.1186/s12886-024-03642-z.

[10] I. D. Zaytsev and G. G. Aseyev, "Properties of Aqueous Solutions of Electrolytes." Taylor & Francis, 1992.

[11] S. A. Mirnezami, M. Rajaei Jafarabadi, and M. Abrishami, "Temperature distribution simulation of the human eye exposed to laser radiation," *Journal of Lasers in Medical Sciences*, vol. 4, no. 4, pp. 175–181, 2013.

[12] K. Ohmi and H.-Y. Li, "Particle-tracking velocimetry with new algorithms," *Measurement Science and Technology*, vol. 11, no. 6, p. 603, Jun. 2000. DOI: 10.1088/0957-0233/11/6/303.

[13] W. Thielicke and E. J. Stamhuis, "PIVlab – towards user-friendly, affordable and accurate digital particle image velocimetry in MATLAB," *Journal of Open Research Software*, 2014. DOI: 10.5334/jors.bl.

[14] W. Thielicke and R. Sonntag, "Particle image velocimetry for MATLAB: Accuracy and enhanced algorithms in PIVlab," *Journal of Open Research Software*, vol. 9, no. 1, p. 12, May 31, 2021. DOI: 10.5334/jors.334.

[15] C. A. Blackie, W. S. Rasband, and K. W. Eliceiri, "NIH image to ImageJ: 25 years of image analysis," *Nature Methods*, vol. 9, no. 7, pp. 671–675, Jul. 2012. DOI: 10.1038/nmeth.2089.

Chapter 4

THERMAL PAD SIZE VARIATION

4.1 Introduction

In this chapter, we investigate how variations in thermal pad size influence the resulting flow field. The base thermal pad (3.0mm thickness) is cut to size and applied directly to the Peltier heater. On top of this thermal pad, a thin black graphite thermal pad (0.07mm thickness) is applied. The base thermal pads were chosen to be 6x6mm and 12x12mm in size. The 6x6mm thermal pad acts as the smallest, physically-realistic point source for a heated eye mask, while the 12x12mm thermal pad encapsulates the entire bottom area of the eye model, as illustrated in Figure 4.1. We performed planar two-component and volumetric three-component flow visualization and measurement experiments, as described in the Experimental Setups and Methods chapter, for each thermal pad size.

The experiment images and data were used to analyze the evolution of the flow field. Additionally, particle pathlines derived from measured two- and three-component velocity fields served to evaluate the effectiveness of each thermal pad in facilitating targeted particle delivery. Finally, a dimensional analysis was conducted to provide a generalized characterization of the flow field.

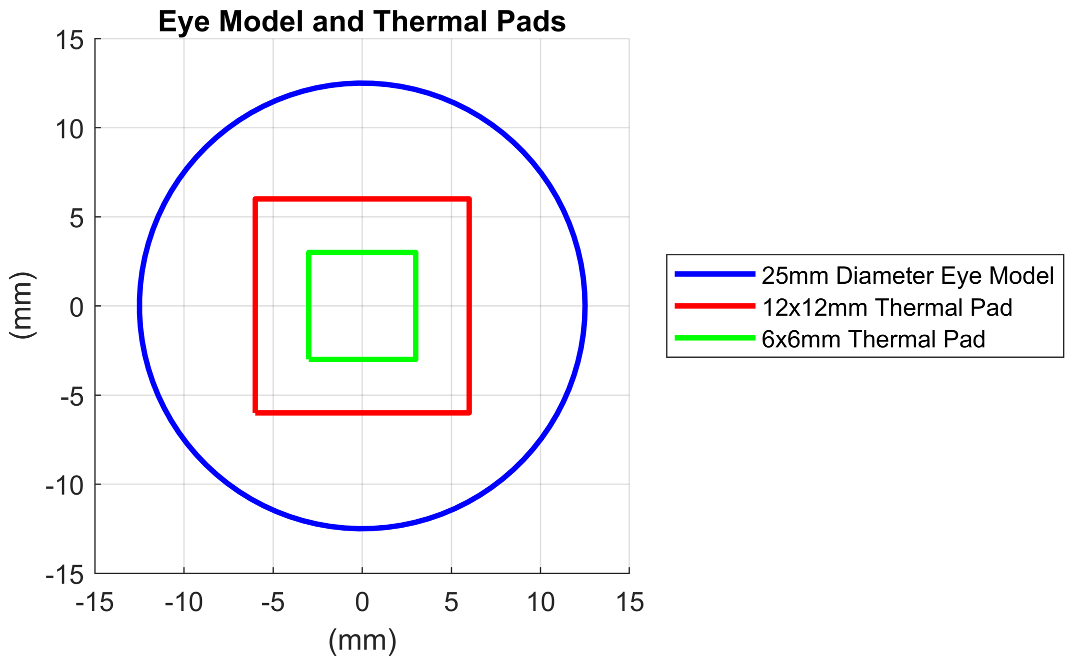

Figure 4.1: Diagram of thermal pad sizes relative to the eye model.

4.2 Unsteady Flow Analysis

Planar Two-Component Experiments

As an initial assessment of the effects of thermal pad size variation on the flow field, we examined the flow fields qualitatively. Short pathlines were created by overlaying the planar experiment images taken at the center of the eye model, as described in the subsection "Qualitative Two-Dimensional Pathlines" in the Experimental Setups and Methods chapter. For each pathline image in this chapter, the accompanying velocity plot is available in Appendix: Thermal Pad Size Variation.

For both thermal pads, just after the heater is turned on, the fluid through the center moves upward slowly, while the fluid on the left and right sides move downward toward the heat source. This creates two vortices in the upper region of the eye model, which can be faintly seen in the first row of images in Figure 4.2. After 15 seconds, two vortices emerge at the bottom of the eye model, by the heater, seen in the second row of images in Figure 4.2. The vortices by the heater grow until they reach the upper vortices. After 20 seconds, four vortices can be seen in the 6x6mm thermal pad pathline image (third row, right image in Figure 4.2). After 40 seconds of heating, the lower counter-rotating vortices have become dominant and cover the entire center plane of the model (fourth row of images in Figure 4.2). The flow has switched direction and moves primarily downward through the center and upward on the left and right sides.

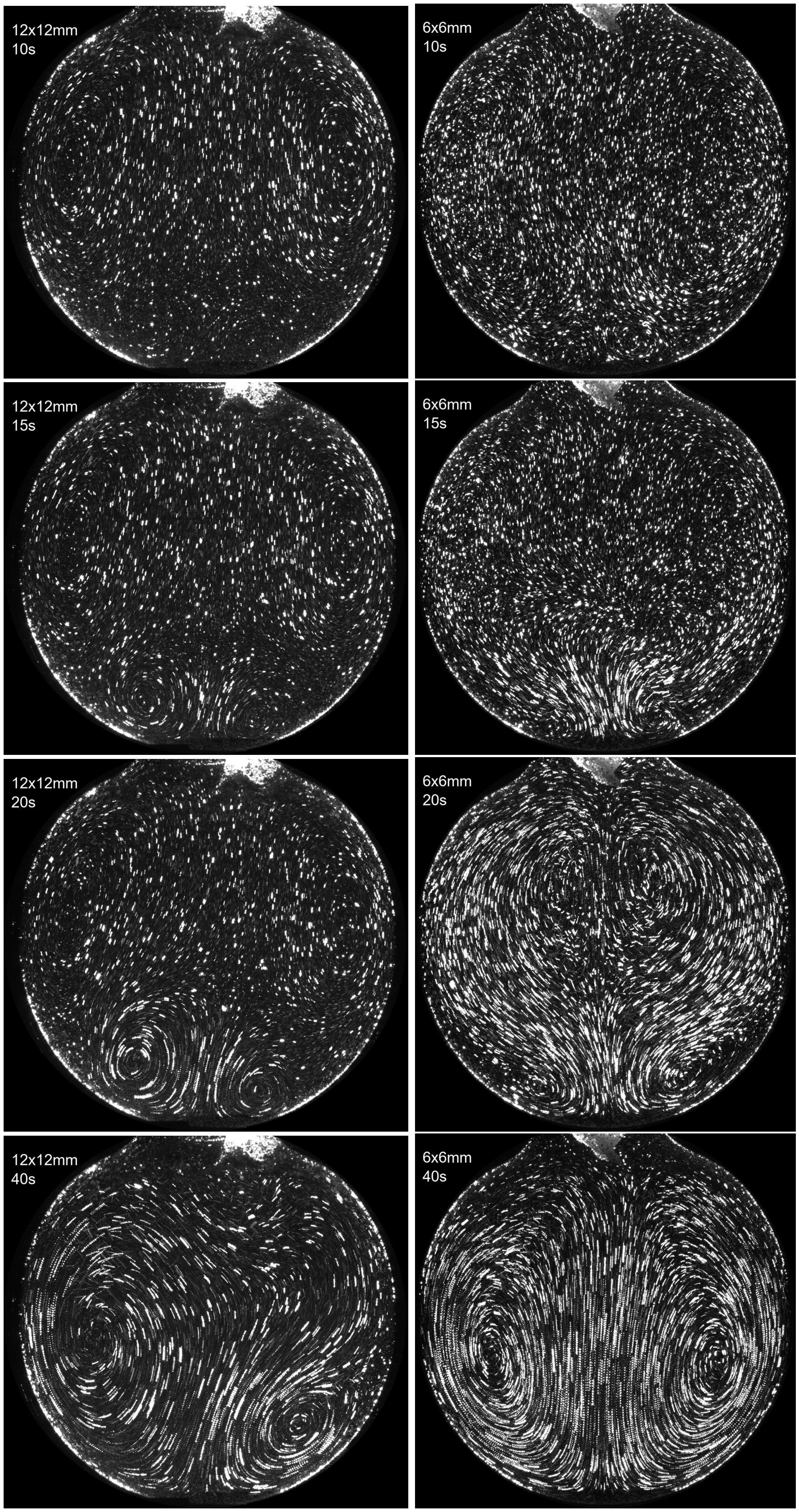

Figure 4.2: Flow pathline images created from 12×12mm (left) and 6×6mm (right) thermal pad experiment images. Rows 1–4 correspond to times of 10s, 15s, 20s, and 40s, respectively.

Volumetric Three-Component Experiments

For a comprehensive picture of the startup stage of the flow field, the volumetric three-component experiments were analyzed. To capture the three-dimensional dynamics in a two-dimensional image, two-dimensional planes were color-coded for velocity magnitude and plotted with the streamlines from the instantaneous three-dimensional velocity field (Figures 4.3 and 4.4). The z-plane located at the center of the eye model ($z = 16.5$) is color coded for v, the vertical velocity component. The two y-planes ($y = 3.5$, $y = -9.5$) are color coded for w, the depth-wise velocity component. The heater is located at approximately $y = -15$, with gravity pointing in the negative y-direction, as shown in Figure 4.3 (a).

For both experiments, shortly after the heater is turned on (1s-10s), the v velocity through the center is positive as the fluid slowly rises while the w velocity component remains weak (Figure 4.3 (a) and (b) and Figure 4.4 (a) and (b)). As the system progresses into the intermediate startup stage (15-20s), the velocity field becomes more structured and intense. After 15 seconds for the 6x6mm thermal pad, and 20 seconds for the 12x12mm thermal pad, the vertical flow through the center switches direction (Figures 4.3 (c) and 4.4 (d)). Two counter-rotating vortices are visible, moving upward along the edges of the eye model and downward through the center. This mirrors observations from the two-dimensional experiments. The streamlines indicate well-defined circulatory motion, while the depth-wise velocity component begins to show more pronounced variations, suggesting enhanced lateral mixing. By the end of the startup phase (40-60s), the velocity fields are fully developed, revealing more complex flow interactions (Figure 4.3 (e) and (f) and Figure 4.4 (e) and (f)). The streamlines and depth-wise velocity components indicate intensified lateral motion, and stronger velocity gradients emerge, particularly in the 12x12mm thermal pad experimental data.

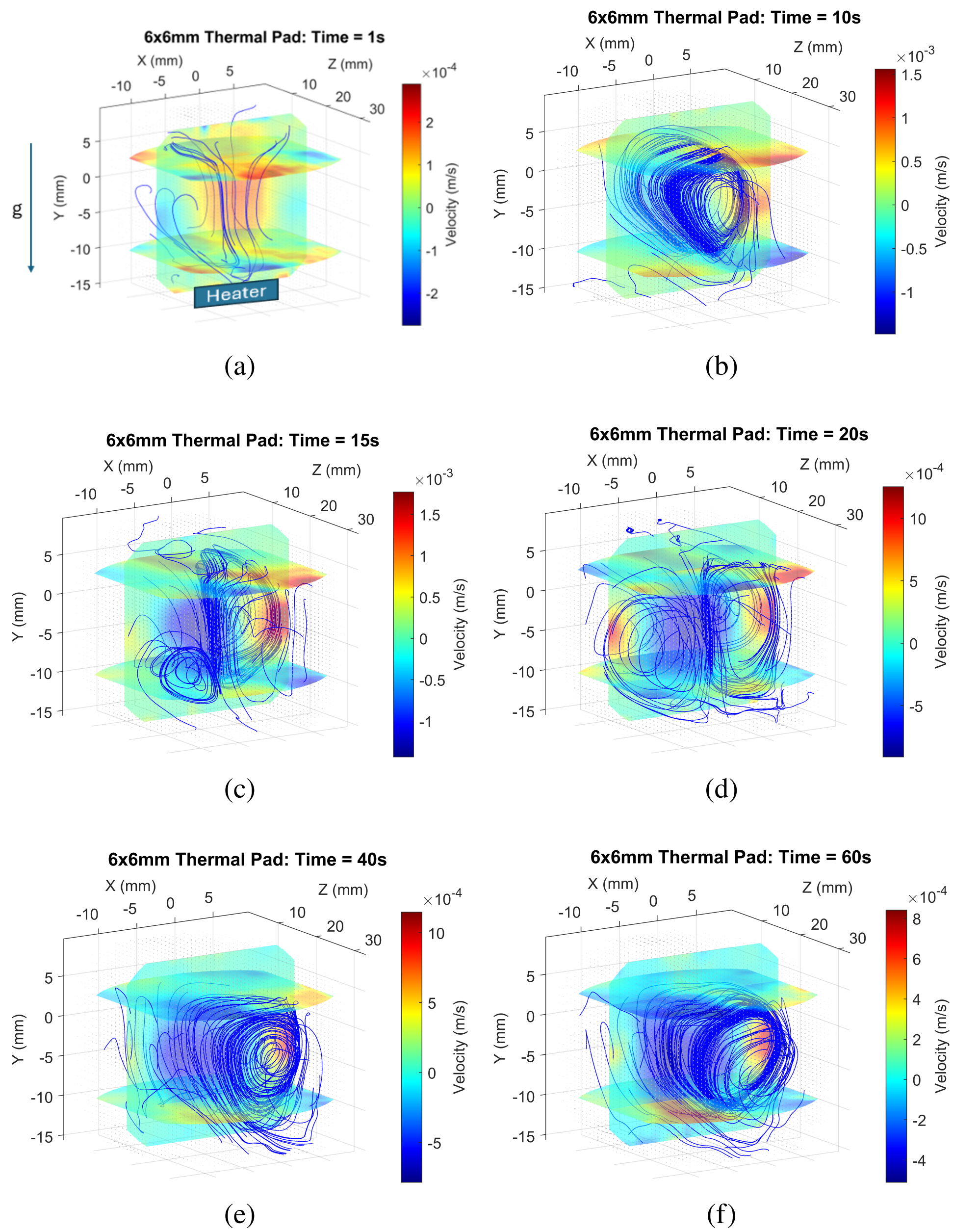

Figure 4.3: Selected planes from the 6x6mm thermal pad three-component volumetric velocity field show the complexity and three-dimensionality of the flow after heating for 1s, 10s, 15s, 20s, 40s, and 60s, corresponding to (a)-(f), respectively.

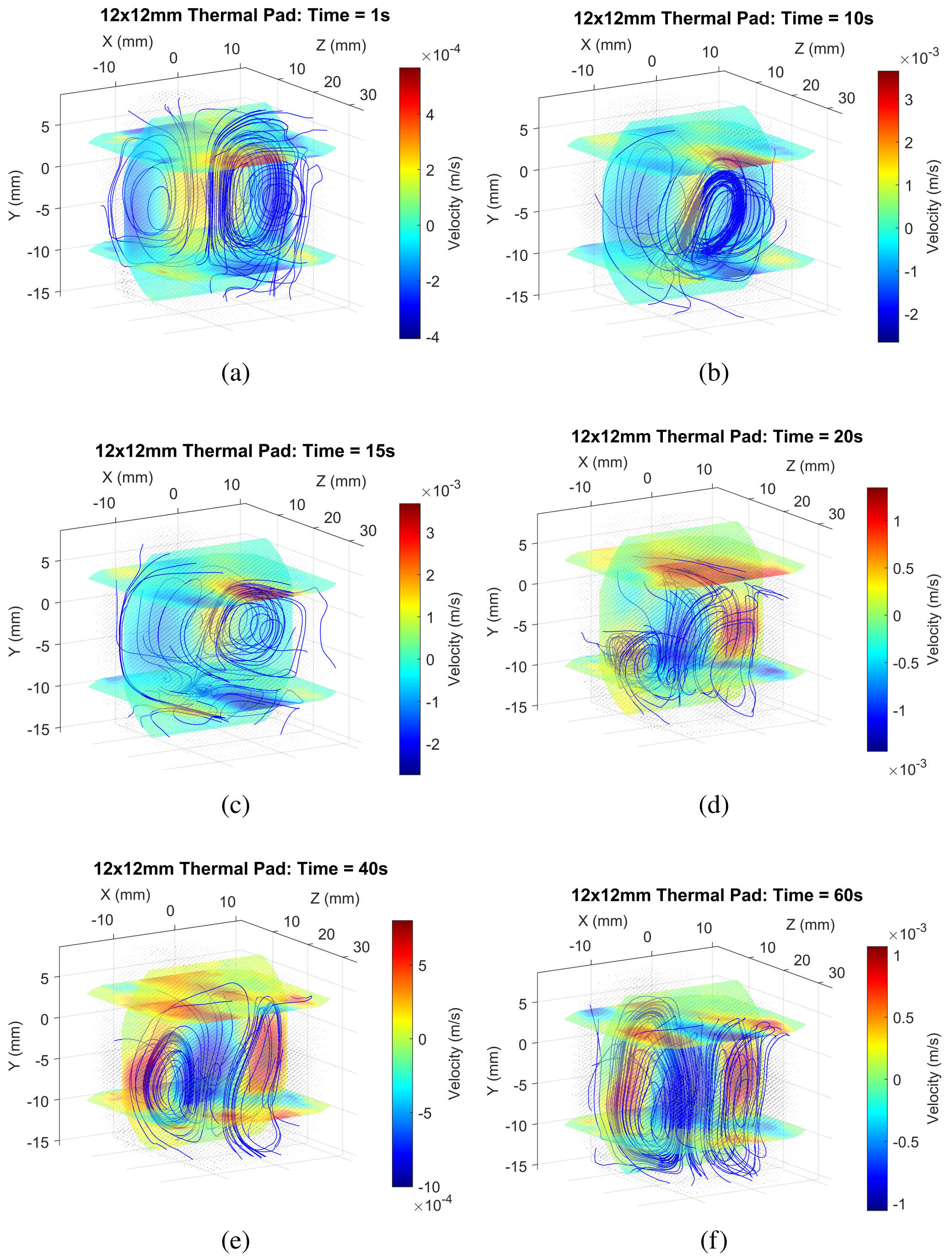

Figure 4.4: Selected planes from the 12x12mm thermal pad three-component volumetric velocity field show the complexity and three-dimensionality of the flow after heating for 1s, 10s, 15s, 20s, 40s, and 60s, corresponding to (a)-(f), respectively.

4.3 Injection Accuracy: Particle Pathline Assessment

After examining the topology and development of the flow fields in two and three dimensions, we evaluated the suitability of each thermal pad size for enhancing particle delivery to the target region. To assess how the thermal pad sizes affect particle trajectories, particle pathlines were examined.

Three-Dimensional Analysis

For the three-dimensional pathline analysis, we "injected" simulated particles into the velocity field obtained from volumetric three-component PTV experiments. Using the velocity field at each time point, we tracked the simulated particles' movement over time.

Ophthalmologists inject relatively close to the front of the eye, 3.5-4mm behind the limbus, angling to the center, and targeting a depth of 7mm. This ensures injection into the vitreous chamber while minimizing the risk of retinal injury [1], [2]. A plane towards the bottom of the eye model, $y = -10$, was chosen accordingly to represent a typical injection plane (Figure 4.5 (b)). The initial positions of the simulated particles are shown in Figure 4.5 (a) and span from $x = [-14 : 7]$ and $z = [10 : 20]$. Sixty-six particles were tracked over the first 300 seconds of heating. A particle was classified as having reached the target area, near the macula, if its position exceeded $y = 1.5$.

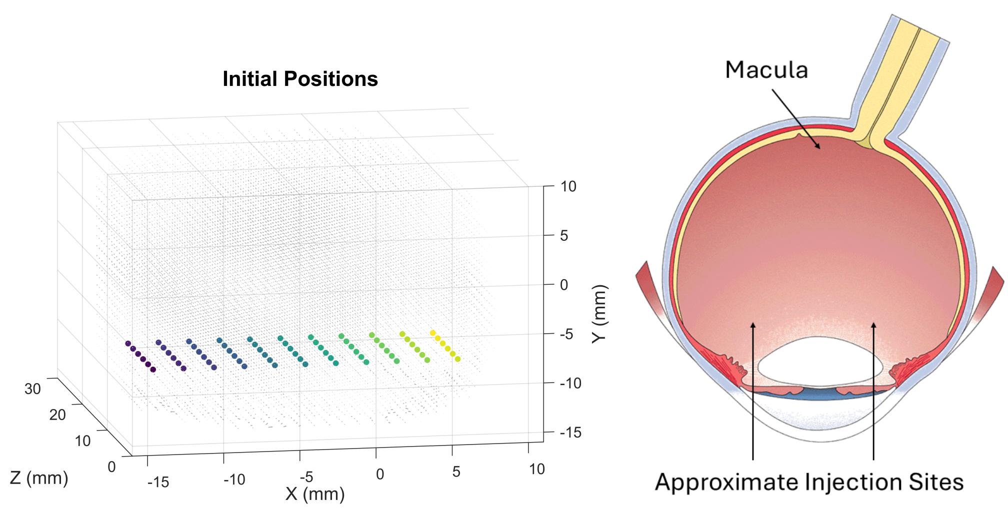

(a) (b)

Figure 4.5: Initial particle positions. (a) Initial positions of the tracked particles in the three-component velocity data, with the left side in purple and the right side in yellow. (b) Diagram of the injection sites relative to the eye.

For the 6x6mm thermal pad experiment, the dominant flow structure is one large vortex (Figure 4.6 (a)), which matches the volumetric velocity plots in the later startup stage (Figure 4.3 (e) and (f)). Most of the particles on the right half of the injection plane reached the target area by 300 seconds of heating (Figure 4.6 (b)). However, examining the pathlines over shorter time periods reveals more complicated flow structures. The pathlines created from 0-30 seconds, illustrated in Figure 4.7 (a), show the particles on the left ($x = -14$) and right ($x = 7$) sides of the injection plane moving in the positive y-direction at the edges of the eye model. The particles in the center ($x = -3.5$) are pushed forward toward $z = 0$ at the front of the eye model. The pathlines from 0-60 seconds show this trend continuing. However, the particles pushed forward in the center begin to split left (negative x-direction) and right (positive x-direction) (Figure 4.7 (b)). The pathlines from 0-120 seconds, displayed in Figure 4.7 (c), show the particles on the right reaching the top of the vortex, then moving back down in the negative y-direction through the center. The particles on the left are pushed forward toward $z = 0$ and downward in the negative y-direction, having never reached the target area. This explains how the initial particles on the left never reach the target area; the center region is split; and all the particles on the right reach the target area.

For the 12x12mm thermal pad experiment, the dominant flow structure, shown in Figure 4.8 (a), is two counter-rotating vortices. Initial particles on both the left ($x = -14$) and right ($x = 7$) sides of the injection plane reached the target area after 300 seconds (Figure 4.8 (b)). The particle pathlines from 0-30s, seen in Figure 4.9 (a), show the particles on the left and right sides moving upward in the positive y-direction. The particles through the center ($x = -3.5$) also move upward but only slightly, before being pushed forward toward $z = 0$. The particle pathlines from 0-60s in Figure 4.9 (b) show, like the 6x6mm thermal pad experiment, the center particles splitting left (negative x-direction) and right (positive x-direction). The particles initially on the left and right sides continue to move upward, reaching the top of their respective vortices, before moving toward the center in the positive and negative x-directions, respectively. The particle pathlines from 0-120s show fully two formed vortices (Figure 4.9 (c)). By 180 seconds, several particles have made multiple rotations around the left vortex, and two particles initially on the right side have become entrained in the left vortex, indicating enhanced mixing (Figure 4.9 (d)).

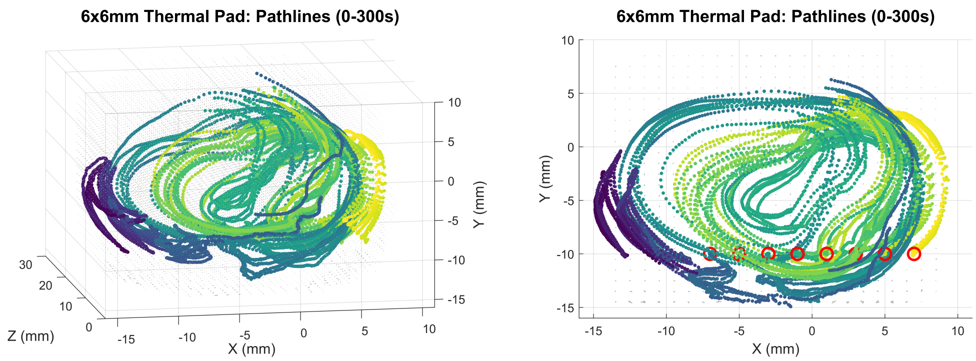

(a) (b)

Figure 4.6: Using three-component data from the volumetric 6x6mm thermal pad experiment, three-dimensional pathlines follow simulated particles from 0-300 seconds. (a) Three-dimensional view of the particle pathlines. (b) Two-dimensional (x-y plane) view of the particle pathlines. Particles that reached the target area are circled in red.

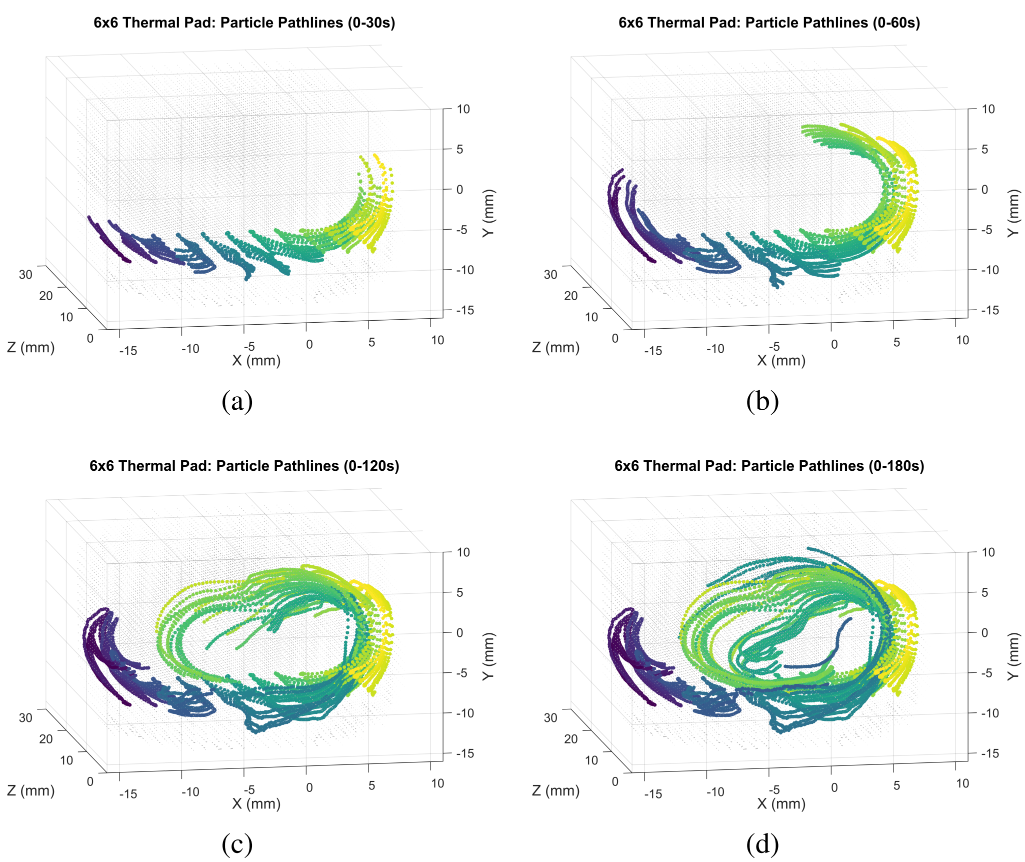

Figure 4.7: Using three-component data from the volumetric 6x6mm thermal pad experiment, three-dimensional pathlines follow simulated particles from (a) 0-30s, (b) 0-60s, (c) 0-120s, and (d) 0-180s.

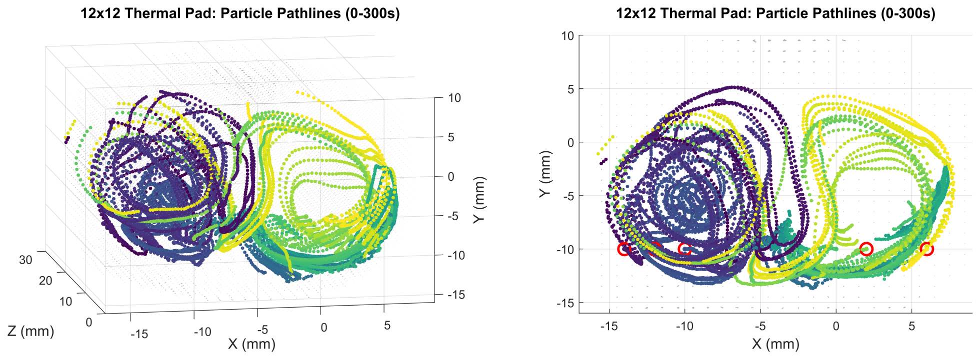

(a) (b)

Figure 4.8: Using three-component data from the volumetric 12x12mm thermal pad experiment, three-dimensional pathlines follow simulated particles from 0-300 seconds. (a) Three-dimensional view of the particle pathlines. (b) Two-dimensional (x-y plane) view of the particle pathlines. Particles that reached the target area are circled in red.

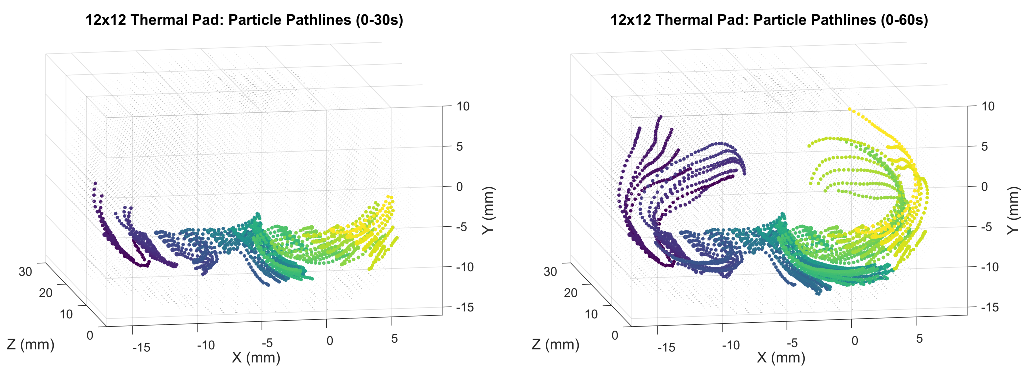

(a) (b)

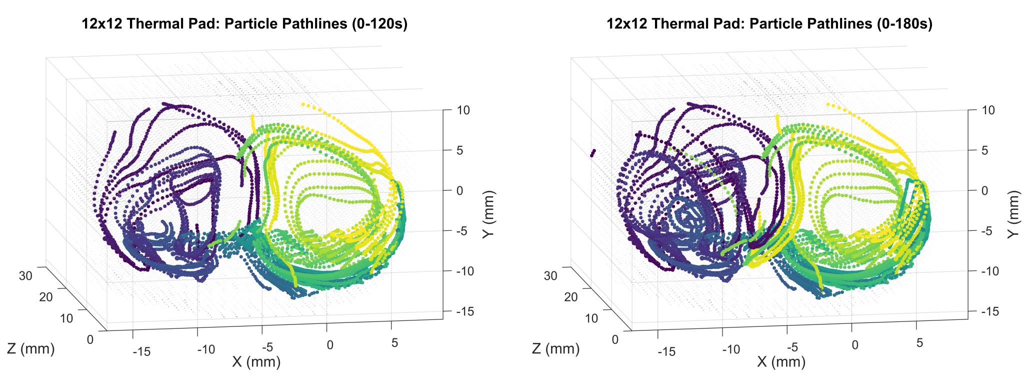

(c) (d)

Figure 4.9: Using three-component data from the volumetric 12x12mm thermal pad experiment, three-dimensional pathlines follow simulated particles from (a) 0-30s, (b) 0-60s, (c) 0-120s, and (d) 0-180s.

Two-Dimensional Analysis

For a more statistical analysis, we "injected" simulated particles into the velocity field obtained from the planar two-component PIV experiments. Using the velocity field at each time point, the simulated particle movement was tracked over time.

Five areas were identified for the simulated injections. The anti-VEGF injection is 0.05-0.07 ml, while the vitreous is 4.5 ml [3]. Accordingly, each simulated injection site corresponded to about 2% of the total eye area. Like the three-component pathline assessment, the initial positions for the simulated injection sites are located towards the bottom of the eye model. The target area, the macula, is located at the top of the eye model. The simulated injection sites and target area are shown in Figure 4.10.

In order to calculate statistics from the injection sites, each location is seeded with approximately 100 simulated particles. The percentage of particles reaching the target area from each injection site is summarized in Tables 4.1 and 4.2. The column, titled "Percentage of Particles to Reach Target Area," denotes the percentage of particles that reached the target area by the end of the heating experiment, at 540 seconds.

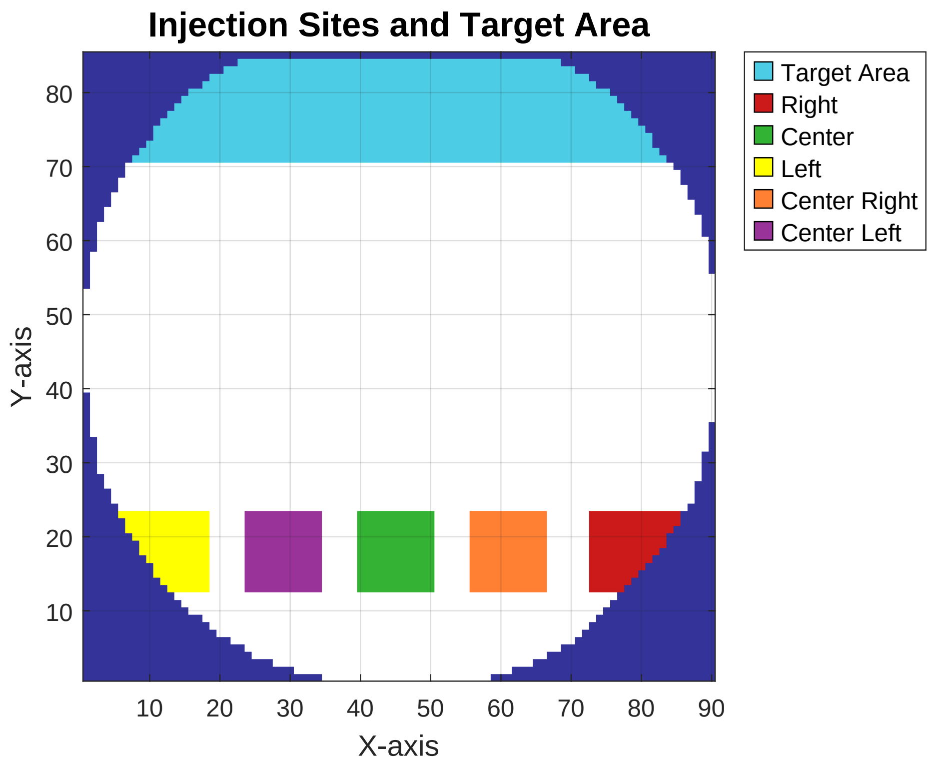

Figure 4.10: Diagram of the target area and injection sites. In this bottom heating configuration, the front of the eye is along $y = 0$, which is also the location of the heater. The top of the eye model, $y = [70 : 85]$ represents the target area, where the macula is located. Injection sites are located towards the front of the eye, along $y = 18$. The x and y-axis dimensions correspond to the grid used in PIVlab.

The two-component particle pathline assessment reveals how thermal pad size affects delivery to the target region. For both the 6x6mm and 12x12mm thermal pads, success delivery to the target region was highly dependent on the initial position of the injection. The injection site at the center of the eye model performed poorly for

Area	Percentage of Particles to Reach Target Area
Left	65
Center Left	4
Center	0
Center Right	35
Right	82.8

Table 4.1: Results from the pathline analysis for the planar two-component 6x6mm thermal pad experiment.

Area	Percentage of Particles to Reach Target Area
Left	52.8
Center Left	74.4
Center	10.7
Center Right	9.92
Right	21

Table 4.2: Results from the pathline analysis for the planar two-component 12x12mm thermal pad experiment.

both thermal pads. This is likely due to the downward flow through the center and upward flow at the outer edges of the eye model, as discussed earlier and shown in Figures 4.3 (c) and 4.4 (d). For the 12x12mm thermal pad, the average percentage of particles reaching the target area across all injection sites is 33.8%, whereas for the smaller 6x6mm thermal pad, the average is slightly higher at 37.4%. The results from the 6x6mm thermal pad, Table 4.1, show a more uneven distribution in percentages, with significant concentrations on the left (65%) and right (82.8%) most injection sites and minimal or no particles reaching in the center (0%) and center-left (4%) regions. This implies that the smaller thermal pad produced a more targeted flow pattern. In contrast, the results from the 12x12mm thermal pad, Table 4.2, show a broader spread of particle delivery across all injection sites, albeit with a notable concentration reaching the target area from the center-left region (74.4%). This suggests that the larger heating surface produced a well-distributed flow pattern throughout the eye model, and ultimately, a more balanced dispersion of particles across the injection sites.

If one could ensure exact injection placement, the 6x6mm thermal pad could be considered more desirable for promoting drug delivery to the macula since a high percentage of particles from the right and left most injection sites reached the target area. However, precise control over the injection site is challenging due to variations between individual patients and the differing technique employed by each ophthalmologist. For this reason, we concluded that the 12x12mm thermal pad, which showed the greatest distribution across all injection sites, may be better suited for promoting particle movement to the target area.

4.4 Dimensional Analysis

To characterize the flow field more broadly, a dimensional analysis was conducted. Dimensional analysis simplifies complex physical problems by reducing the number of independent variables into dimensionless groups that capture the system's essential physics, enabling results to be generalized across scales and conditions. For our experiment, there are nine key physical variables:

$$f(L, U, \rho, \mu, \beta, g, \Delta T, k, C_p) = 0$$

where:

- L = Characteristic length (m) $[L]$
- U = Characteristic velocity (m/s) $[L][T]^-1$
- ρ = Density (kg/m^3) $[M][L]^-3$
- μ = Dynamic viscosity (Pa·s or kg/(m·s)) $[M][L]^-1[T]^-1$
- β = Thermal expansion coefficient (1/K) $[\Theta]^-1$
- g = Gravitational acceleration (m/s^2) $[L][T]^-2$
- ΔT = Temperature difference (K) $[\Theta]$
- k = Thermal conductivity (W/(m·K)) $[M][L][T]^-3[\Theta]^-1$
- C_p = Specific heat capacity (J/(kg·K)) $[L]^2[T]^-2[\Theta]^-1$.

There are four fundamental dimensions: length, time, temperature difference, and mass noted by $[L]$,$[T]$,$[\Theta]$, and $[M]$, respectively. The Buckingham Pi theorem states that a physically meaningful equation involving n physical variables and k fundamental dimensions can be reduced to a set of $n - k$ dimensionless groups. In our case, $n = 9$ and $k = 4$, therefore, five dimensionless groups are predicted. They are as follows:

The Prandtl number describes the ratio of momentum diffusivity (viscous effects) to thermal diffusivity (heat conduction) in a fluid. A low Prandtl number indicates that thermal diffusion is faster than momentum diffusion, while a higher Prandtl number denotes momentum diffusion dominates. The Prandtl number (Pr) is defined as:

$$\Pi_1 : \mathrm{Pr} = \frac{\mu}{\alpha\rho} = \frac{C_p\mu}{k}. \tag{4.1}$$

The Prandtl number introduces a new variable, thermal diffusivity (α). Thermal diffusivity is a material property that describes how quickly heat spreads through a material. The following relation is used as a substitution for α:

$$\alpha = \frac{k}{\rho c_p}. \tag{4.2}$$

The Péclet number describes the relative importance of advection (transport by fluid motion) versus diffusion (spread by molecular conduction) in heat and mass transport. A high Péclet number indicates that convection dominates, and a low Péclet number denotes that diffusion is the dominate transport. The Péclet number (Pe) is defined as:

$$\Pi_2 : \mathrm{Pe} = \frac{UL}{\alpha} = \frac{L\rho C_p U}{k}. \tag{4.3}$$

The Rayleigh number is often used in buoyancy-driven flows. The Rayleigh number characterizes the flow regime; above a certain value signifies turbulent flow, below that value denotes laminar flow. A very low Rayleigh number signifies that there is no fluid motion, and heat transfer is by conduction rather than convection. The Rayleigh number (Ra) is defined as:

$$\Pi_3 : \mathrm{Ra} = \frac{g\,\beta\,\Delta T\,L^3\,\rho^2\,c_p}{\mu\,k}. \tag{4.4}$$

The Reynolds number describes the flow regime. A low Reynolds number indicates laminar flow while a high Reynolds number denotes turbulent flow. The Reynolds number represents the ratio of inertial forces to viscous forces. The Reynolds number (Re) is defined as:

$$\Pi_4 : Re = \frac{\rho UL}{\mu}. \tag{4.5}$$

The Nusselt number is the ratio of convective heat transfer to conductive heat transfer at a boundary in a fluid. It characterizes the efficiency of heat transfer. A Nusselt number of one indicates heat transfers by pure conduction. A Nusselt number greater than one signifies that conductive heat transfer is aided by convection, and a high Nusselt number corresponds to active convection. The Nusselt number (Nu) is defined as:

$$\Pi_5 : Nu = \frac{hL}{k}. \tag{4.6}$$

The convective heat transfer coefficient (h) is not a fixed physical property of a material. It depends on the conditions of the experimental setup, such as fluid velocity and surface geometry. Due to this dependence on external factors, h is often solved for empirically. Previous studies have developed correlations for the Nusselt number for specific conditions [4]–[7]. For our experiment, we consider the correlation developed by [8]. Their experimental study was on the convective heat transfer in liquids confined between two horizontal plates and heated from below. The tested fluids, water, mercury, and silicone oils of varying viscosities, covered Rayleigh numbers from 1.51×10^5 to 6.76×10^8 and Prandtl numbers from 0.02 to 8750. The results indicated that all tested liquids follow a common correlation based on Prandtl and Rayleigh number. We use this correlation to estimate the Nusselt number of our system:

$$\Pi_5 : Nu = 0.069 \cdot (Ra)^{1/3} \cdot (Pr)^{0.074}. \tag{4.7}$$

In calculating the dimensionless numbers, it is important to note that some physical properties of 55% NaI solution are not readily available in the literature. The viscosity, thermal conductivity, and density are interpolated values from [9]. The specific heat value is extrapolated from lower concentrations of NaI solutions, such as 44% and 46% NaI, from [9].

In the absence of published values, the coefficient of volumetric thermal expansion is estimated using the density of 55% NaI solution at different temperatures. The coefficient of volumetric thermal expansion (β) describes how the volume of a substance changes with temperature at a constant pressure:

$$\beta = \frac{1}{V}\left(\frac{\partial V}{\partial T}\right)_P. \tag{4.8}$$

Starting with the relation between density (ρ) and volume (V):

$$V = \frac{1}{\rho}. \tag{4.9}$$

Taking the derivative with respect to temperature:

$$\frac{\partial V}{\partial T} = -\frac{1}{\rho^2}\frac{\partial \rho}{\partial T}. \tag{4.10}$$

Substituting Equation 4.10 into Equation 4.8 to get the relation between density and the coefficient of thermal expansion:

$$\beta = -\frac{1}{\rho}\left(\frac{\partial \rho}{\partial T}\right)_P. \tag{4.11}$$

Using discrete values for temperature and density:

$$\beta \approx -\frac{1}{\rho_1} \cdot \frac{\rho_2 - \rho_1}{T_2 - T_1}. \tag{4.12}$$

Finally, β can be determined by substituting the density values of 55% NaI solution at two temperatures. The values for the physical properties of 55% NaI solution can be found in Table 4.3. For the characteristic velocity, U, we calculated the mean of the vertical velocity component, v, over the course of the 12x12mm planar two-component experiment. For the characteristic length scale, L, when calculating the Rayleigh and Péclet numbers, we use the radius, as is often used in the literature [10], [11]. This choice reflects the distance over which temperature-induced density variations drive convective currents within the sphere as well as the scale over which heat is transported by fluid motion relative to the rate of thermal diffusion. For the Reynolds number, the eye model's diameter is used. The diameter accounts for the largest flow structures that develop as fluid circulates within the entire volume of the sphere. The physical variables that are characteristic of the experimental setup can be found in Table 4.4.

C_p (KJ/kg·K)	2135
μ (mPa·s)	2.155
k (W/m·K)	0.464
ρ (kg/m^3)	1654
β (10^{-4}/K)	4.67

Table 4.3: Physical properties for 55% NaI solution at 20°C.

L ($10^{-}3$ m) [Rayleigh, Péclet]	12.5
L ($10^{-}3$ m) [Reynolds]	25
U ($10^{-}4$ m/s)	3.85
θ (K)	3
g (m/s^2)	9.81

Table 4.4: Physical variables of the experiment.

Pr	Pe	Ra	Re	Nu
9.9	36.6	1.57×10^5	7.4	4.4

Table 4.5: Calculated dimensionless numbers for our system.

The calculated dimensionless numbers are shown in Table 4.5. The Rayleigh number of our system is 1.57×10^5. This value exceeds the critical threshold of approximately 1708 for the classical Rayleigh–Bénard convection, where a layer of viscous fluid between two smooth horizontal plates is heated at the bottom wall and cooled at the top [12]. The Rayleigh number of our system indicates the presence of natural convection. It remains below the range typically associated with turbulent flow (10^6), indicating that the system operates within a laminar convection regime [12].

The Prandtl number of our system is 9.9, representing the ratio of momentum diffusivity to thermal diffusivity. This value, greater than one, implies that the momentum boundary layer is larger than the thermal boundary layer. For liquids composed of simple molecules (as opposed to liquid metals or complex molecules like oils made of long-chain hydrocarbons), the Prandtl number is typically on the order of 1 to 10 [13].

The Reynolds number was calculated to be 7.4, indicating that the flow is laminar. In this regime, viscous forces are dominant over inertial forces.

The Péclet number of our system is 36.6, signifying the relative importance of convective to conductive heat transfer. Values greater than one indicate that convection plays a stronger role in heat transport within the system.

Finally, the Nusselt number was determined to be 4.4. This dimensionless number indicates the efficiency of heat transfer through convection relative to pure conduction. A Nusselt number greater than one confirms that convective heat transfer is present.

In summary, the calculated dimensionless numbers collectively indicate that the system operates within a laminar natural convection regime. Momentum diffusivity exceeds thermal diffusivity, resulting in a thicker momentum boundary layer compared to the thermal boundary layer. The Rayleigh number confirms the presence of natural convection, where the thermal instabilities induce oscillations, vortices, and an unsteady flow pattern, without reaching turbulent conditions. Additionally, the dominance of convective heat transfer over conduction, as indicated by the Péclet and Nusselt numbers, highlights the efficient thermal transport. These findings signify that convection significantly enhances heat and mass transfer while maintaining laminar flow.

4.5 Conclusion

This chapter investigated how variations in thermal pad size influence the flow field. Planar two-component and volumetric three-component flow measurements enabled a comprehensive spatial and temporal characterization of the evolving flow structures.

Pathline-based injection simulations were conducted to evaluate the effectiveness of each thermal pad size for targeted delivery. Both thermal pads induced fluid mixing, as evidenced by successful particle transport from the left and right injection sites. However, the 12x12mm thermal pad enabled particle delivery to the target area from all injection sites, suggesting it may be better suited for drug delivery applications. Dimensional analysis provided a broader context for interpreting the flow behavior, confirming that the system operates within a laminar natural convection regime.

Chapter References

[1] D. Yorston, "Intravitreal injection technique," *Community Eye Health*, vol. 27, no. 87, p. 47, 2014.

[2] Z. Oztas, C. Akkin, F. Afrashi, and S. Nalcaci, "The short-needle intravitreal injection technique," *International Journal of Ophthalmology*, vol. 9, no. 6, pp. 929–930, Jun. 18, 2016. DOI: 10.18240/ijo.2016.06.24.

[3] A. M. Azhdam, R. A. Goldberg, and S. Ugradar, "In vivo measurement of the human vitreous chamber volume using computed tomography imaging of 100 eyes," *Translational Vision Science & Technology*, vol. 9, no. 1, p. 2, Jan. 2020. DOI: 10.1167/tvst.9.1.2.

[4] J. D. Hall, A. Bejan, and J. B. Chaddock, "Transient natural convection in a rectangular enclosure with one heated side wall," *International Journal of Heat and Fluid Flow*, vol. 9, no. 4, pp. 396–404, Dec. 1988. DOI: 10.1016/0142-727X(88)90006-9.

[5] E. N. Sieder and G. E. Tate, "Heat transfer and pressure drop of liquids in tubes," *Industrial & Engineering Chemistry*, vol. 28, no. 12, pp. 1429–1435, Dec. 1, 1936. DOI: 10.1021/ie50324a027.

[6] F. W. Dittus, "Heat transfer in automobile radiators of the tubular type," *International Communications in Heat and Mass Transfer*, vol. 12, no. 1, pp. 3–22, 1985. DOI: 10.1016/0735-1933(85)90003-X.

[7] S. W. Churchill and H. H. Chu, "Correlating equations for laminar and turbulent free convection from a vertical plate," *International Journal of Heat and Mass Transfer*, vol. 18, no. 11, pp. 1323–1329, Nov. 1975. DOI: 10.1016/0017-9310(75)90243-4.

[8] S. Globe and D. Dropkin, "Natural-convection heat transfer in liquids confined by two horizontal plates and heated from below," *Journal of Heat Transfer*, vol. 81, no. 1, pp. 24–28, Feb. 1, 1959. DOI: 10.1115/1.4008124.

[9] I. D. Zaytsev and G. G. Aseyev, "Properties of Aqueous Solutions of Electrolytes." Taylor & Francis, 1992.

[10] S. Weinbaum, "Natural convection in a horizontal circular cylinder," *Journal of Fluid Mechanics*, vol. 18, no. 3, p. 409, Mar. 1964. DOI: 10.1017/S0022112064000313.

[11] H. H. Bau and K. E. Torrance, "Low rayleigh number thermal convection in a vertical cylinder filled with porous materials and heated from below," *Journal of Heat Transfer*, vol. 104, no. 1, pp. 166–172, Feb. 1, 1982. DOI: 10.1115/1.3245045.

[12] K. R. Sreenivasan and J. J. Niemela, "Turbulent convection at very high rayleigh numbers and the weakly nonlinear theory," *Atmosphere*, vol. 14, no. 5, p. 826, May 4, 2023. DOI: 10.3390/atmos14050826.

[13] J. H. Lienhard and J. H. Lienhard, “A heat transfer textbook,” 5th Ed. Mineola (NY): Dover Publications, Inc, 2019.

Chapter 5

[INTENTIONALLY REDACTED FOR PROPRIETARY REASONS]

Chapter 6

PHYSICS-INFORMED NEURAL NETWORK: EXTRACTIONS FROM PLANAR DATA

6.1 Introduction

As described in the previous chapters, volumetric three-component particle tracking velocimetry is an advanced experimental technique that requires minimal optical distortion, precise camera calibration and alignment, and high computational power for image processing and three-dimensional particle reconstruction and tracking. From our complex experimental setup, we acquired volumetric three-component flow measurements for different heating configurations, capturing the unsteady buoyancy-driven flow throughout the eye model.

In this chapter, we investigated whether a Physics-Informed Neural Network (PINN), trained on data acquired through simpler planar experimental techniques, can predict a volumetric flow field. PINNs propose a unique use-case for environments where data may be limited but can be extrapolated with the aid of governing equations. We developed a PINN that trains on three spatially-sparse planes of three-component data, extracted from the volumetric 12x12mm thermal pad particle tracking velocimetry experimental data. The training planes for our PINN could alternatively be acquired through stereoscopic particle image velocimetry (stereo-PIV), a more accessible experimental method that is easier to set up and less computationally expensive. We test the capabilities of the PINN to predict and reconstruct additional planes of velocity data, comparing the PINN output to planes from our volumetric three-component experimental velocity field. A successful reconstruction using PINNs could break ground in novel, inexpensive flow visualization and measurement methods.

6.2 PINN Architecture Overview

In line with the original paper conceptualizing PINNs [1], the Deep Neural Network (DNN) takes the following form as a Multi-Layer Perceptron:

$$(\mathbf{U}, p, T) = f_{NN}(\mathbf{X}, t; \Theta) \tag{6.1}$$

where:

- $\mathbf{U}$ = u, v, w (horizontal, vertical, and depth-wise) velocity components
- p = Pressure
- T = Temperature
- f_{NN} = Neural network
- $\mathbf{X}$ = x,y,z spatial input coordinates
- t = Temporal coordinates
- Θ = All trainable parameters.

Figure 6.1 displays a schematic of the PINN architecture. The network used in this study has 12 layers and 32 nodes. A tanh activation function was selected for all layers, due to its simplicity and continuous differentiability. Additionally, the learning rate is updated over specific epochs, beginning with $\lambda_0 = 5 \cdot 10^{-3}$, and following a exponential decay schedule. The values for the learning rate λ, and the epochs at which they are updated, were chosen empirically based on the progression of the loss over training. Finally, based on contemporary practices, the Adam optimizer [2] was chosen for the model, and the neural network weights were initialized with a Xavier Uniform initialization [3].

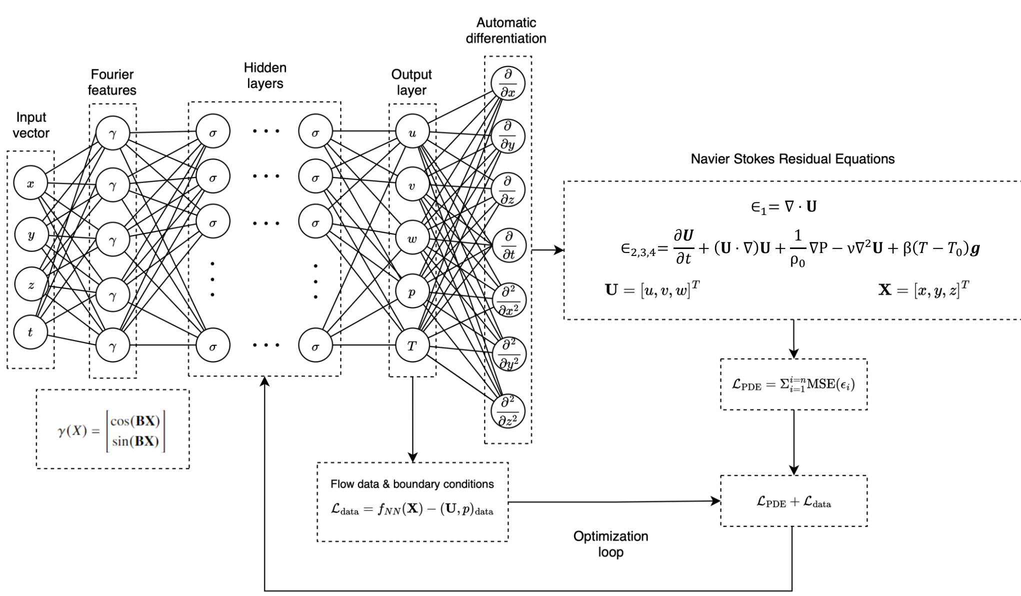

Figure 6.1: Schematic diagram depicting the PINN architecture used in this study.

By courtesy of [4] and [5], some additional implementations have been included in this PINN architecture. The input parameters $\mathbf{X}$ are non-dimensionalized to $(\mathbf{X}, \mathbf{U}) \in [0, 1]$, which has been shown to improve convergence and diminish discrepancies across multiple scales. Furthermore, the same authors recommended the implementation of random Fourier features, using the following encoding before being passed through the DNN:

$$\gamma(X) = \begin{bmatrix} \cos(\mathbf{BX}) \\ \sin(\mathbf{BX}) \end{bmatrix} \tag{6.2}$$

where $\mathbf{B}$ is a gaussian sampling following the distribution $\mathcal{N}(0, \sigma^2)$ and σ is an additional hyperparameter $\sigma \in [1, 10]$. This implementation improved representation of larger gradients as well as convergence. The propensity for neural networks to suffer from spectral bias is well studied, and the inclusion of random Fourier features significantly mitigates this [6]. The value of σ is user-defined and in this study a value of $\sigma = 2$ has been shown to produce optimal results [5].

6.3 PINN Loss Function

The total loss function of our PINN model combines the loss calculated from the experimental data ($\mathcal{L}_{data}$), boundary conditions ($\mathcal{L}_{BC}$), and governing equations ($\mathcal{L}_{PDE}$), to train the neural network by minimization of the loss landscape during backpropagation. The loss contributions are defined as:

$$\mathcal{L}_{data} = \sum_{i=1}^{N_{data}} |\mathbf{U}_{data}(\mathbf{X}^i) - \mathbf{U}_{pred}(\mathbf{X}^i)|^2 \tag{6.3}$$

$$\mathcal{L}_{BC} = \sum_{i=1}^{N_{BC}} |\mathbf{U}_{BC}(\mathbf{X}^i) - \mathbf{U}_{pred}(\mathbf{X}^i)|^2 \tag{6.4}$$

$$\mathcal{L}_{PDE} = \sum_{i=1}^{N_{PDE}} |\mathcal{L}_i(\mathbf{X}^i)|^2 \tag{6.5}$$

where $\mathbf{U}_{data}$ and $\mathbf{U}_{pred}$ are the measured and predicted velocity fields, respectively. N_{data}, N_{BC}, and N_{PDE} are the number of experimental data measurements, boundary conditions, and PDEs, respectively. $\mathcal{L}_{data}$, $\mathcal{L}_{BC}$, and $\mathcal{L}_{PDE}$ are calculated using the mean-squared error function. For $\mathcal{L}_{BC}$, a no-slip condition was prescribed at the boundaries of the glass eye model to represent the viscous effects at the surface.

For the governing equations, the unsteady Navier-Stokes equations with Boussinesq approximation model the flow. The central assumption of the Boussinesq approximation is that density variations are sufficiently small to be neglected, except in the buoyancy term of the momentum equation, where they drive natural convection. The derivation of the Boussinesq approximation and a discussion of its validity in this study is available in Appendix: Physics-Informed Neural Network. The governing equations for our system, the incompressible continuity equation and unsteady momentum equation with Boussinesq approximation are defined as:

$$\epsilon_1 = \nabla \cdot \mathbf{U} \tag{6.6}$$

$$\epsilon_2, \epsilon_3, \epsilon_4 = \frac{\partial \mathbf{U}}{\partial t} + (\mathbf{U} \cdot \nabla)\mathbf{U} + \frac{1}{\rho_0}\nabla p - \nu \nabla^2 \mathbf{U} + \mathbf{g}\beta(T - T_0) \tag{6.7}$$

where:

- ρ_0 = Initial density
- p = Pressure
- T = Temperature
- T_0 = Initial temperature
- ν = Kinematic viscosity
- β = Coefficient of thermal expansion.

Differentiation is performed using PyTorch's automatic differentiation function [7], which is capable of efficiently obtaining the necessary partial derivatives for every parameter at every iteration. ϵ_1, ϵ_2, ϵ_3, and ϵ_4 are the PDE residuals that contribute to $\mathcal{L}_{PDE}$, where the momentum equation is calculated in the x, y, and z-directions.

The total loss function of the neural network is defined as:

$$\mathcal{L} = (1 - \alpha) \cdot (\mathcal{L}_{data} + \mathcal{L}_{BC}) + \alpha \cdot \mathcal{L}_{PDE} \tag{6.8}$$

where α denotes a weighting factor that monitors the contribution of each loss. In this study, a value of $\alpha = 0.1$ was used, based on findings in literature as well as trial and error showing this to produce the most accurate results [5], [8]–[11].

6.4 Collocation Points and Training

The collocation points where the PDE residuals are evaluated are shown in Figure 6.2 (a), alongside the surface of the reconstructed eye-model, where the boundary conditions are prescribed (Figure 6.2 (b)). The number of points used for enforcing the boundary conditions and to a greater extent the governing equations (collocation points) greatly affect the outcome of the training cycle. A sufficient concentration of collocation points is required to obtain an accurate approximation of the partial derivatives through the autograd function. In this investigation, 100,000 collocation points were utilized, and one-tenth were dedicated to the fulfillment of boundary conditions. The need to retain the gradients of each variable at each collocation point greatly impacts the computational requirement (GPU), and delivers a trade-off between remaining NN parameters, such as the size and depth of the PINN.

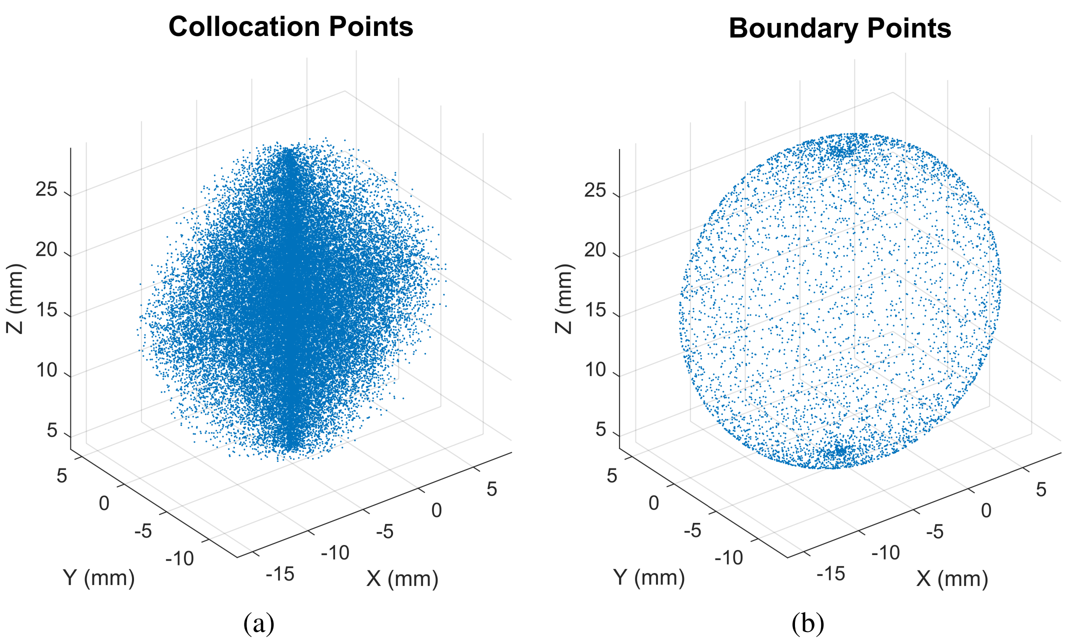

Figure 6.2: Collocation and boundary condition points are shown in (a) and (b), respectively. Collocation points are where PDE residuals are calculated, and boundary points are where the no-slip condition is enforced.

The PINN is trained on three planes of three-component PTV data, extracted from the volumetric 12x12mm thermal pad experimental data. The training planes are shown in Figure 6.3. The training planes are located at $z = [10.5, 16.5, 22.5]$. The time duration for the training data spans from 25 to 35 seconds after the heater was turned on. This was chosen as a particularly unsteady period in the flow field. These z-planes were selected for their experimental accessibility; velocity measurements could be acquired using a stereo-PIV setup with a traverse set to move the eye model 6mm in the depth-wise direction after each run, for a total of three runs.

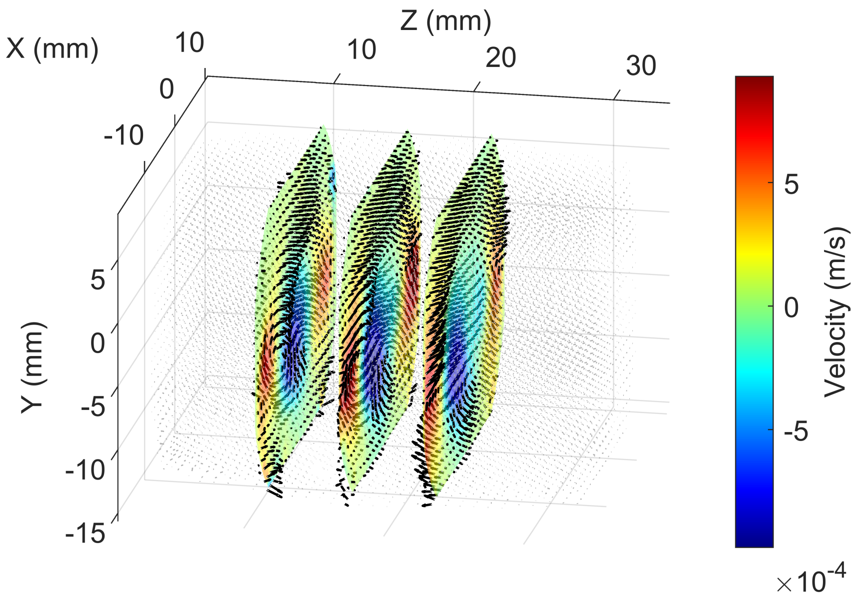

Figure 6.3: Experimental two-dimensional three-component PTV data used for training the PINN is located at three distinct planes along the z-axis. The planes are color-coded according to the magnitude of v, the vertical velocity component. The velocity field at 25 seconds after the heater was turned on is shown in this plot.

The total loss function is calculated and recorded while training. Figure 6.4 shows the loss function plotted over epochs. Given our α value, the $\mathcal{L}_{data}$ is weighted heavily in the total loss function and its large contribution is illustrated in Figure 6.4. Residual equations 1-4 are calculated from continuity, x-momentum, y-momentum, and z-momentum equations, respectively. The boundary loss, while important in establishing the effects of viscous surfaces and boundary layer development, must be limited in its contribution to the total loss function due to the propensity of the PINN to optimize towards a trivial solution, where all velocities are zero.

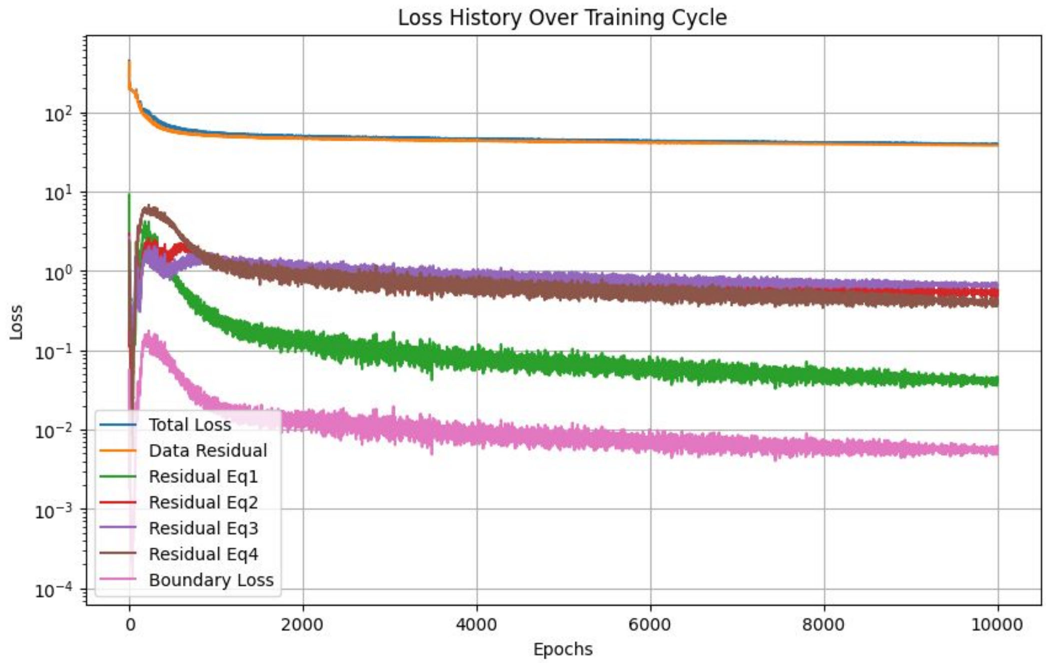

Figure 6.4: Plot showing the loss function over epochs. Residual equations 1-4 correspond to continuity, x-momentum, y-momentum, and z-momentum.

6.5 Results

Two planes were chosen for testing, as shown in Figure 6.5. The testing planes were located at $z = 13.5$, positioned between two training planes, and at $y = -3.5$. For comparison, the experimental data is shown alongside the PINN output in Figures 6.6 and 6.7. The z-plane is color-coded for the magnitude of v, the vertical velocity component (Figure 6.6), while the y-plane is color-coded for the magnitude of w, the depth-wise velocity component (Figure 6.7).

For the z-plane, the velocity plot from the experimental data reveals two dominant counter-rotating vortices, with positive vertical velocity concentrated on the left and right, and negative vertical velocity through the center (Figure 6.6 (a)). The PINN prediction captures the overall structure and symmetry of the flow field, successfully reproducing the dual vortex pattern (Figure 6.6 (b)). The PINN output appears more continuous. In the experimental velocity field, the contour plot showing the velocity magnitude appears patchy, particularly on the right ($x = [0 : 8]$, $y = [0 : 6]$), whereas the PINN output displays a smooth and connected velocity field. Several outliers appear in the experimental velocity field, especially on the bottom right of the field of view ($x = [4 : 6]$, $y = [-14 : -12]$), which are smoothed out in the PINN output. Overall, the PINN accurately captures the large-scale flow dynamics

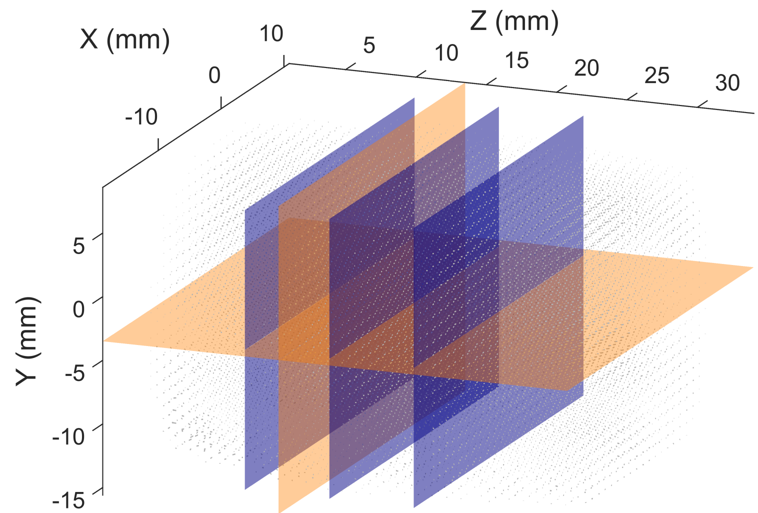

Figure 6.5: Plot showing the training planes in blue and testing planes in orange.

and demonstrates strong agreement with the experimental data.

For comparison to the PINN output, we performed a linear interpolation of the experimental data, interpolating between the $z = [10.5, 16.5]$ planes to get the interpolated velocity field at $z = 13.5$ (Figure 6.6 (c)). The contour plot for the interpolated velocity field is patchier than the experimental and PINN plots. Significant outliers are visible on the right ($x = [7 : 8]$, $y = [0 : 3]$). Minor outliers appear on the bottom left ($x = [-17 : -13]$, $y = [-14 : -12]$). This interpolated velocity field, with its outliers, highlights the PINN's ability to both predict and smooth the velocity field.

For the y-plane, the experimental data (Figure 6.7 (a)) exhibits a distinctive flow pattern. The plot shows a negative depth-wise velocity component through the center, indicating that the flow moves from the back of the eye model forward through the center of this plane. This matches observations from the three-dimensional particle pathline assessment in the Thermal Pad Size Variation Chapter, where the particles in the center were pushed forward (Figure 4.9 (a)). The contour plot for the experimental data is patchy and fragmented. The PINN prediction captures the overall structure and complexity of the flow field, successfully reproducing the broader back to front pattern through the center (Figure 6.7 (b)). The contour plot for the PINN output is smoother than the experimental data, with some errors where the velocity gradients are especially pronounced, for example $x = [3 : 7]$, $z = [25 : 27]$.

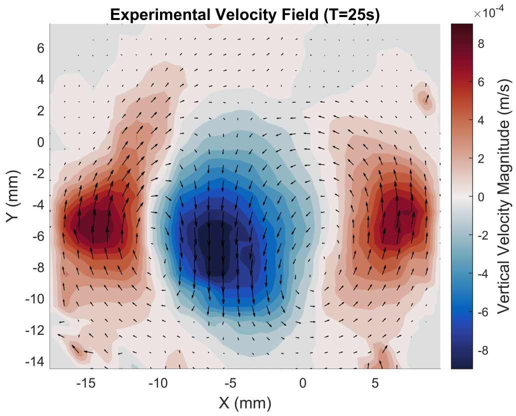

(a)

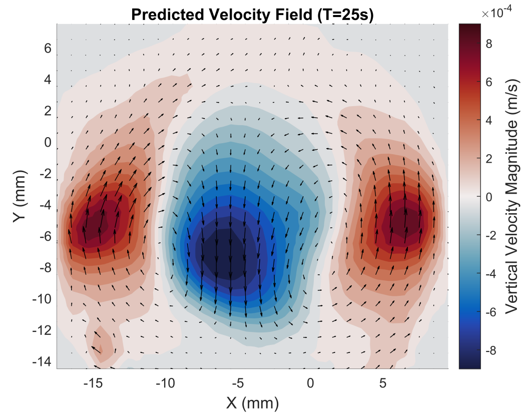

(b)

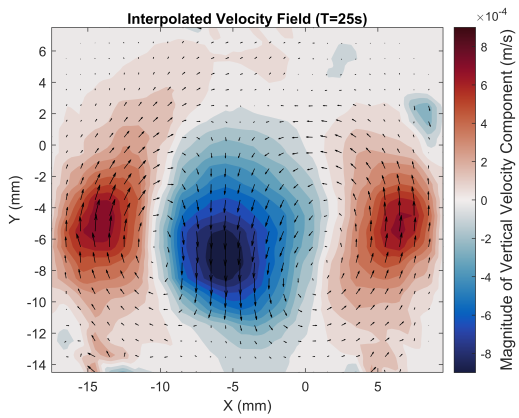

(c)

Figure 6.6: Velocity plots for the $z = 13.5$ plane, showing (a) the experimental data, (b) the PINN output, and (c) the interpolated velocity field at 25 seconds after the heater is turned on.

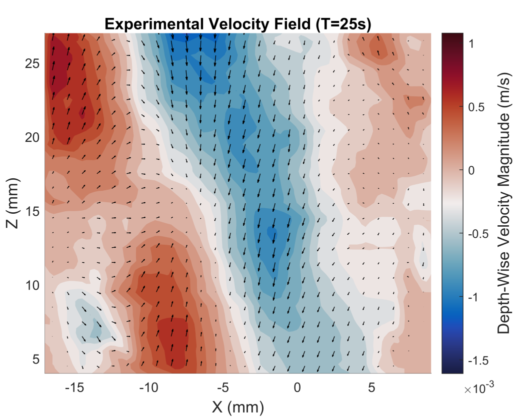

(a)

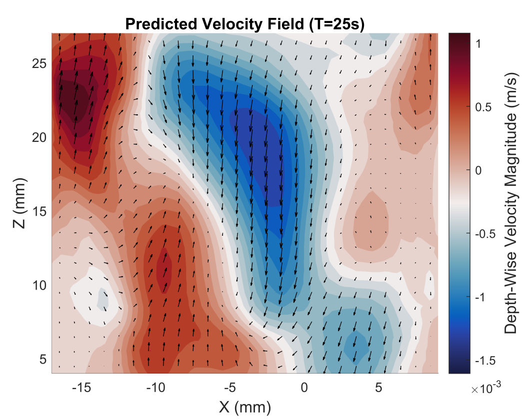

(b)

Figure 6.7: Velocity plots for the $y = -3.5$ plane, showing (a) the experimental data and (b) the PINN output at 25 seconds after the heater is turned on.

6.6 Conclusion

In this chapter, we developed a PINN that trains on three separate planes of three-component velocity data. The training data was chosen for its ability to be acquired through simpler experimental methods, like stereo-PIV. The loss function for the model combines the loss from data, boundary conditions, and physical relations, with the data loss being weighted heavily. The unsteady Navier-Stokes equations with Boussinesq approximation were used for the system's governing equations, and a no-slip condition was enforced at the boundaries of the eye model.

The outputs from the PINN closely matched the experimental data for the x-y plane at $z = [13.5]$. This result highlights the potential for a PINN to reduce the number of runs of stereo-PIV experiments needed to capture z-plane velocity profiles. While the output from the PINN did not match the experimental data as closely for the $y = -3.5$ plane, the results are noteworthy. The y-plane data would be difficult to measure experimentally, requiring either a second stereo-PIV setup, with cameras located above the eye model facing downward towards it, or a complete volumetric three-component experimental setup. The results from the y-plane suggest that a PINN could potentially be used in place of complex flow visualization techniques, particularly when the goal is to capture broader flow dynamics. Further PINN development strategies are discussed in the subsequent chapter.

Chapter References

[1] M. Raissi, P. Perdikaris, and G. E. Karniadakis, "Physics-informed neural networks: A deep learning framework for solving forward and inverse problems involving nonlinear partial differential equations," *Journal of Computational physics*, vol. 378, pp. 686–707, Feb. 2019.

[2] D. P. Kingma and J. Ba, "Adam: A method for stochastic optimization," 2017. arXiv: 1412.6980.

[3] X. Glorot and Y. Bengio, "Understanding the difficulty of training deep feedforward neural networks," in *Proceedings of the Thirteenth International Conference on Artificial Intelligence and Statistics*, vol. 9, May 2010, pp. 249–256.

[4] S. Wang, H. Wang, and P. Perdikaris, "On the eigenvector bias of fourier feature networks: From regression to solving multi-scale pdes with physics-informed neural networks," *Computer Methods in Applied Mechanics and Engineering*, vol. 384, Oct. 2021. DOI: 10.1016/j.cma.2021.113938.

[5] S. Wang, S. Sankaran, H. Wang, and P. Perdikaris, "An expert's guide to training physics-informed neural networks," 2023. arXiv: 2308.08468.

[6] N. Rahaman, A. Baratin, D. Arpit, *et al.*, "On the spectral bias of neural networks," 2019. arXiv: 1806.08734.

[7] A. Paszke, S. Gross, F. Massa, *et al.*, "Pytorch: An imperative style, high-performance deep learning library," 2019. arXiv: 1912.01703.

[8] S. Wang, X. Yu, and P. Perdikaris, "When and why PINNs fail to train: A neural tangent kernel perspective," *Journal of Computational Physics*, vol. 449, Jan. 15, 2022. DOI: 10.1016/j.jcp.2021.110768.

[9] S. Wang, Y. Teng, and P. Perdikaris, "Understanding and mitigating gradient pathologies in physics-informed neural networks," 2020. arXiv: 2001.04536.

[10] L. McClenny and U. Braga-Neto, "Self-adaptive physics-informed neural networks using a soft attention mechanism," 2022. arXiv: 2009.04544.

[11] S. Maddu, D. Sturm, C. L. Müller, and I. F. Sbalzarini, "Inverse-dirichlet weighting enables reliable training of physics informed neural networks," 2021. arXiv: 2107.00940.

Chapter 7

CONCLUSION AND FUTURE WORKS

In this study, we examined buoyancy-driven flow within a spherical geometry, with a focus on its relevance to intravitreal drug delivery. In the first chapter, we discussed relevant eye diseases, intravitreal injections, and previous studies on convective transport for drug delivery in the eye. Chapter 2 focused on the vitreous humor and the technique we employed to identify a representative vitreous model that matched both the viscosity in the human vitreous and the refractive index of the eye model. For our refractive index matching analysis, we imaged a calibration grid through the eye model submerged in various candidate fluids. By measuring the apparent displacement of the grid dots, we determined 55% NaI solution to be a well-matched and representative vitreous model.

The third chapter detailed the experimental setup and software used for two-component PIV and three-component PTV measurements. Chapter 4 explored the impact of thermal pad size on the resulting flow field and particle trajectories. While both thermal pad sizes induced convective flow, through a particle pathline assessment, we determined that the larger thermal pad (12x12mm) may be better suited for drug delivery, due to its broader particle distribution to the target area.

In the sixth chapter, we investigated, using our experimental data, whether a PINN, trained on data acquired through planar experimental techniques, can predict a volumetric flow field. Outputs from the PINN, trained on three planes of three-component velocity data, matched the broader flow dynamics of the experimental data at additional testing planes.

Looking forward, there are several avenues to expand upon the work presented in this thesis.

In regards to the PINN, further development and testing is possible. One notable feature of PINNs is their ability to denoise experimental data [1], [2], a capability also observed in the smooth PINN outputs of Chapter 6. A direction for future work is using the PINN as a replacement for the outlier-filling step described in the Experimental Setups and Methods chapter. Additionally, further fine-tuning of the neural network hyperparameters may produce more accurate velocity field predictions. Lastly, we are currently testing the PINN's ability to handle unsteady flows. In Chapter 6, we demonstrated the PINN's ability to accurately predict the velocity field when trained on sparse spatial data. Ongoing work involves training the PINN on temporally sparse data, such as velocity fields at 20 seconds and 30 seconds, and evaluating its ability to predict flow fields at intermediate time points (e.g., at 25 seconds). If successful, this could potentially reduce the computational load of the experiments. For example, if the PINN accurately predicts the velocity field when trained on data taken at every other second, a lower camera frame rate could possibly be used, which would also reduce image processing times.

A promising next step following the particle pathline assessments presented in the Thermal Pad Size Variation Chapter is to perform a fluid mixing analysis using the finite-time Lyapunov exponent (FTLE). Time-dependent flows often exhibit emergent patterns that strongly influence tracer transport. From a trajectory-based perspective, these patterns are known as Lagrangian coherent structures (LCS), which act as transport barriers separating regions of distinct flow behavior. Unlike Eulerian descriptions that provide velocity at fixed spatial points, LCS identify material surfaces that persist over time, offering insight into the organization of unsteady flows [3]–[5]. The FTLE field is a fundamental tool for detecting LCS. The FTLE measures the rate of separation between nearby fluid particles over a finite time interval. Ridges in the FTLE field correspond to regions of maximal stretching, indicating the presence of LCS. Calculating FTLE fields from the experimental data would complement the particle pathline assessments: while pathlines reveal which initial positions reach the target area, the FTLE field, by highlighting transport barriers, can help explain why.

A direction for future work that would help guide experimental design is developing numerical simulations that model the experimental buoyancy-driven flow system. A computational framework would enable rapid testing of alternative heating configurations, such as variations in heater placement. Simulations could help identify optimal configurations for targeted delivery, which could then be tested experimentally.

Future investigations could also refine the physical eye model used in this study to more closely replicate the anatomy of the human vitreous. Adjustments to the model geometry and the inclusion of non-liquefied regions would allow for more a realistic characterization of drug transport. However, developing accurate experimental models of the vitreous is an active area of research [6]–[8]. A more practical next step would be performing these heating experiments on animal eyes. This would be critical to determining the efficacy of using heat to improve drug delivery in the vitreous. The subsequent step, after safety and efficacy are verified, would be clinical trials with patients suffering from AMD, DME, or PDR.

To conclude, this study demonstrated, using an in-vitro vitreous model, that heat could potentially be used to induce convective flow, accelerate drug delivery, and ultimately, improve patient outcomes. We hope this conclusion inspires researchers to consider other minimally-invasive techniques to improve drug delivery.

Chapter References

[1] H. Gao, L. Sun, and J.-X. Wang, "Super-resolution and denoising of fluid flow using physics-informed convolutional neural networks without high-resolution labels," *Physics of Fluids*, vol. 33, no. 7, Jul. 2021. DOI: 10.1063/5.0054312.

[2] H. Eivazi, Y. Wang, and R. Vinuesa, "Physics-informed deep-learning applications to experimental fluid mechanics.," 2024. arXiv: 2203.15402.

[3] G. Haller, "Lagrangian coherent structures," *Annual Review of Fluid Mechanics*, vol. 47, no. 1, pp. 137–162, Jan. 3, 2015. DOI: 10.1146/annurev-fluid-010313-141322.

[4] S. C. Shadden, F. Lekien, and J. E. Marsden, "Definition and properties of lagrangian coherent structures from finite-time lyapunov exponents in two-dimensional aperiodic flows," *Physica D: Nonlinear Phenomena*, vol. 212, no. 3, pp. 271–304, Dec. 2005. DOI: 10.1016/j.physd.2005.10.007.

[5] S. C. Shadden, J. O. Dabiri, and J. E. Marsden, "Lagrangian analysis of fluid transport in empirical vortex ring flows," *Physics of Fluids*, vol. 18, no. 4, Apr. 1, 2006. DOI: 10.1063/1.2189885.

[6] H. Aliyar, W. Foster, P. Hamilton, and N. Ravi, "Towards the development of an artificial human vitreous," *Polymer Preprint*, vol. 45, Jan. 1, 2004.

[7] Q. Lin, J. Y. C. Lim, K. Xue, X. Su, and X. J. Loh, "Polymeric hydrogels as a vitreous replacement strategy in the eye," *Biomaterials*, vol. 268, Jan. 2021. DOI: 10.1016/j.biomaterials.2020.120547.

[8] S. Donati, S. M. Caprani, G. Airaghi, *et al.*, "Vitreous substitutes: The present and the future," *BioMed Research International*, 2014. DOI: 10.1155/2014/351804.

Appendix: Experimental Setup

To ensure the reproducibility of our results and to support future research efforts, we have provided the complete processing settings for two-component planar PIV using PIVlab and volumetric three-component PTV using Insight V3V 4G Software for Volumetric 3-Component Velocimetry Flow Measurement Systems.

PIVlab Settings

PIV algorithm	Multipass FFT window deformation
Correlation robustness	Standard (recommended)
Sub-pixel estimator	Gauss 2x3-point
Interrogation area [px]	52
Step [px]	26

Table .1: PIV settings used with PIVlab.

Insight V3V Settings for Calibration Images

For the calibration images, the images were loaded using the Image Tools tab, one camera at a time, and the traverse position, position step size, and Pixel X and Y were assigned 0, 2, 3.45, and 3.45, respectively.

Step	Processing Type	Settings		
1	Image Calculator	Subtraction: 5		
2	Image Filter	Kernel type: Gaussian	Filter Size: 21	Filter parameter: 0.5

Table .2: Settings used for pre-processing calibration images with the V3V software.

Particle Identification	
Feedback Level	1
Intensity Threshold	20
Origin Type	1
Approximate Point Radius	5
Local Mean Subtraction Size	21
Calibration Point Fitting Method	1
Calibration Configuration	
Feedback Level	1
Calibration Point Spacing (mm)	2
X-Y Axes Definition	3,-1,1
Z Axes Definition	negative
Calibration Target Distances (mm)	unused
Degree of Mapping Functions	auto

Table .3: Settings used for processing calibration images with the V3V software.

Insight V3V Settings for Experiment Images

The experiment images from all three cameras were loaded simultaneously into the software using the Image Tools tab, and "Tiff tags" were assigned to the images. The Delta T was set to 10,000 microseconds, and Pixel X and Y were both set to 3.45 micrometers.

<table>
<tr><th>Step</th><th>Processing Type</th><th colspan="3">Settings</th></tr>
<tr><td>1</td><td>Image Generator</td><td colspan="3">Minimum Intensity</td></tr>
<tr><td>2</td><td>Image Calculator</td><td colspan="3">Subtraction of generator image</td></tr>
<tr><td>3</td><td>Image Filter</td><td>Kernel type: Gaussian</td><td>Filter Size: 5</td><td>Filter parameter: 0.5</td></tr>
<tr><td>4</td><td>Image Calculator</td><td colspan="3">Subtraction: 10</td></tr>
<tr><td>5</td><td>Image Calculator</td><td colspan="3">Multiplication: 1.1</td></tr>
</table>

Table .4: Settings used for pre-processing experiment images with the V3V software.

DPIR Processing	
Feedback Level	1
Number of Passes	1
Initial Matching Tolerance (pix)	0.5
Utilize Time-Resolved Data	0
Advanced Settings	default
Particle Identification	
Feedback Level	1
Intensity Threshold	8
Particle Image Settings	1,6,1.5
Large Object Segmentation Settings	off
Particle Matching	
Feedback Level	1
Final Match Tolerance (pix)	2
Smart Matching	disabled
Volume Depth Bounds (mm)	default
Camera Exclusion	none
Particle Tracking	
Feedback Level	1
Particle Tracking Algorithm	1
Algorithm Settings	0.3, 8, 6, 0.3, 3, 1, 10
Filter: Universal Median Thesholds	2,5
Filter: Global Range	-0.1,0.1,-0.1,0.1,-0.1,0.1
Volume Size (mm)	30,30,30
User-defined Origin (mm)	0,0,0
Time Specifications (milliseconds)	default
Time-Resolved Paths	2,2,0.05
Create Paths with Existing Vectors	0
Output invalid vectors	0
Velocity Interpolation	
Feedback Level	1
Node Volume Dimensions (mm)	2,2,2
Node Volume Overlap (%)	50
Minimum Grid Coordinates (mm)	-15,-15,1
Maximum Grid Coordinates (mm)	9.5,9.5,32.5
Minimum Number of Particles	1
Adaptive Grid	0
Filter: Universal Median Thresholds	3
Smoothing Factor	2
Use Ensemble Interpolation	0
Use Path Interpolation	0
Gridded Hole Filling	0
Gridded Hole Filling Neighborhood Size	0

Table .5: Settings used for processing experiment images with the V3V software.

Appendix: Thermal Pad Size Variation

Velocity over Time

The velocity plots included here aim to supplement the particle pathline images in Chapter 4: Thermal Pad Size Variation. The velocity field was calculated using PIVlab. The contour plots are color-coded according to the magnitude of the vertical velocity component, v.

In the earlier stages (10s-20s), the vertical velocity through the center is positive for both the 12x12mm and 6x6mm thermal pad experiments. After about 40 seconds of heating, the vertical velocity through the center changes direction, with negative vertical velocity through the center and positive vertical velocity on the left and right, as discussed in the Thermal Pad Size Variation chapter.

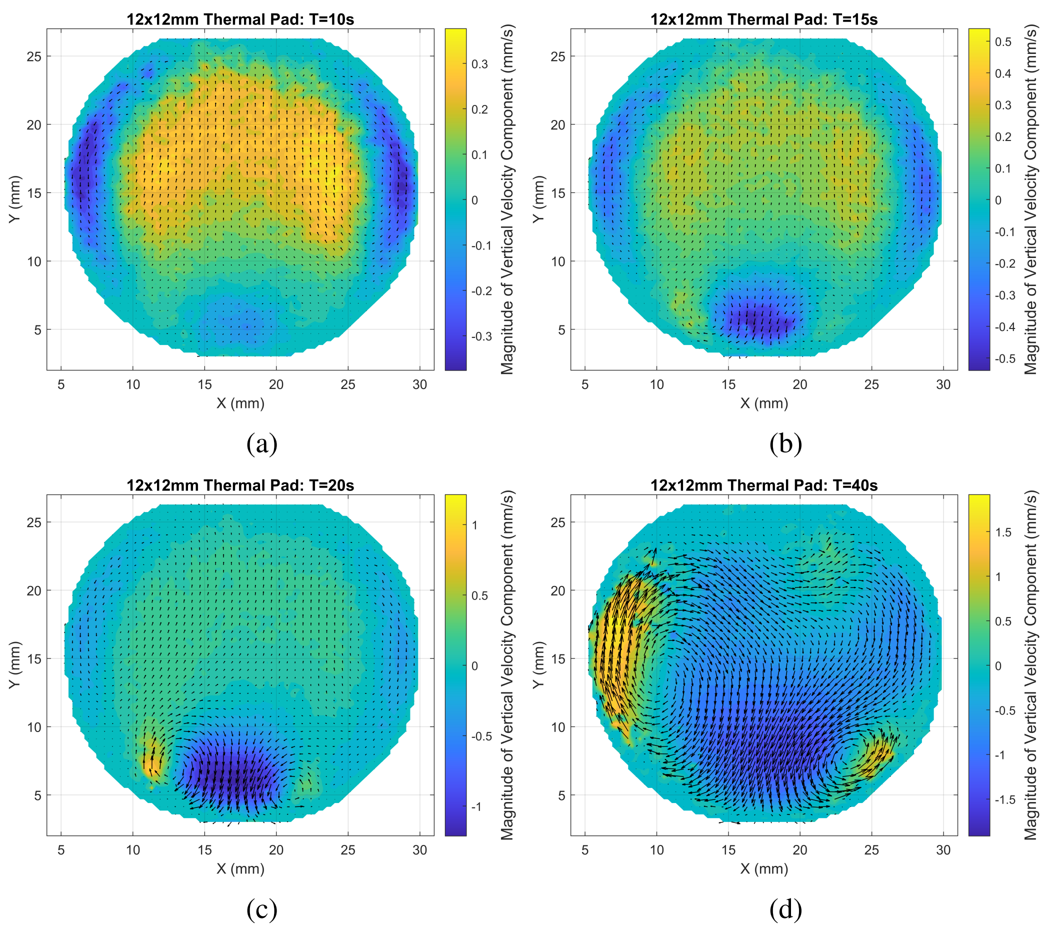

Figure .1: Velocity plots from the 12x12mm thermal pad heating experiment. (a)–(f) correspond to times 10s, 15s, 20s, and 40s, respectively.

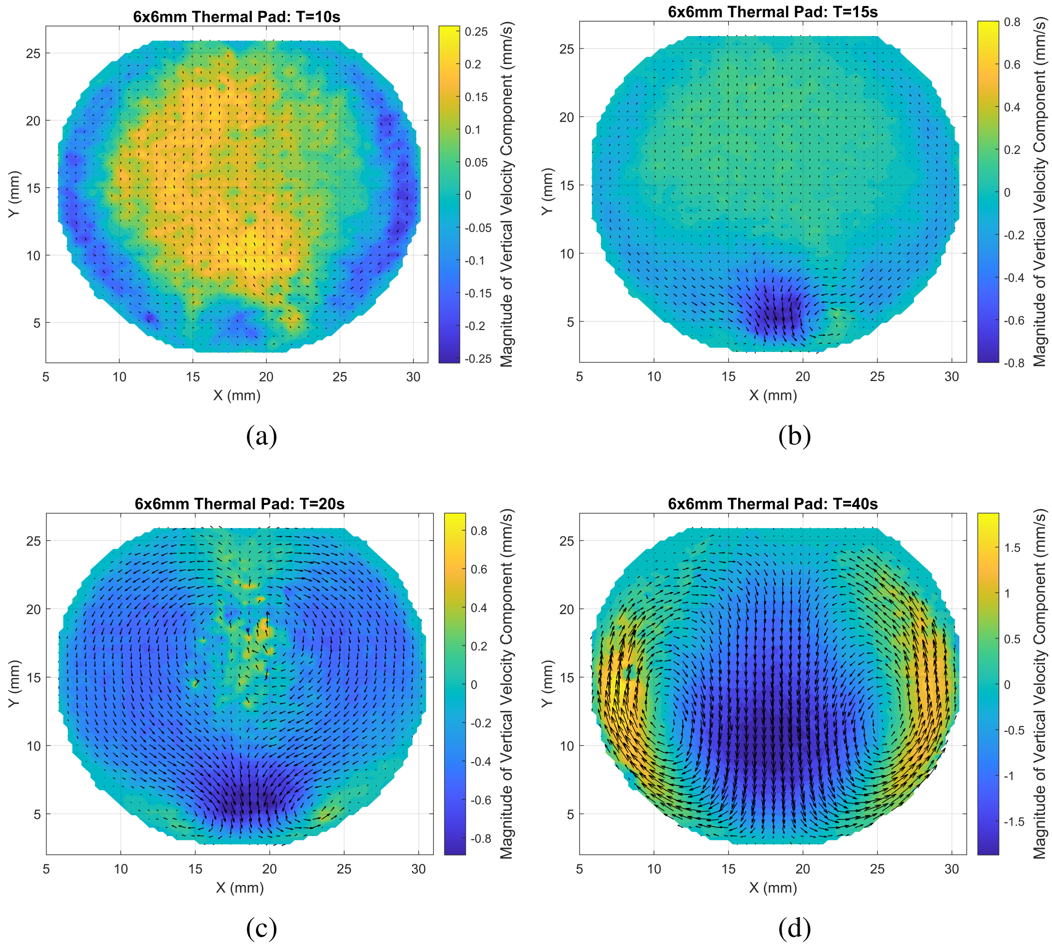

Figure .2: Velocity plots from the 6x6mm thermal pad heating experiment. (a)-(f) correspond to times 10s, 15s, 20s, and 40s, respectively.

Appendix: Physics-Informed Neural Network

Boussinesq Approximation

The Boussinesq approximation is often used for modeling buoyancy-driven flows due to its reduced computational cost compared to solving the full compressible Navier-Stokes equations. The central assumption of the Boussinesq approximation is that density variations are sufficiently small to be neglected, except in the buoyancy term of the momentum equation, where they drive natural convection.

To derive the Boussinesq approximation, start with the compressible continuity equation:

$$\frac{\partial \rho}{\partial t} + \nabla \cdot (\rho \mathbf{u}) = 0. \tag{1}$$

Since density is treated as constant in temporal and convection terms, continuity reduces to:

$$\nabla \cdot \mathbf{u} = 0. \tag{2}$$

Moving to the conservation of momentum, we start with the full compressible form:

$$\frac{\partial (\rho \mathbf{u})}{\partial t} + \nabla \cdot (\rho \mathbf{u} \otimes \mathbf{u}) = -\nabla p + \nabla \cdot \left[\mu \left(\nabla \mathbf{u} + (\nabla \mathbf{u})^T \right) - \frac{2}{3} \mu (\nabla \cdot \mathbf{u}) \mathbf{I} \right] + \rho \mathbf{g}. \tag{3}$$

After assuming viscosity, μ, is constant, plugging in 2, and treating density as constant (ρ_0) except for the gravity term:

$$\rho_0 \left(\frac{\partial \mathbf{u}}{\partial t} + \mathbf{u} \cdot \nabla \mathbf{u} \right) = -\nabla p + \mu \nabla^2 \mathbf{u} + \rho \mathbf{g}. \tag{4}$$

Introducing the coefficient of thermal expansion, β, which is defined as the relative change in density with respect to temperature at constant pressure:

$$\beta = -\frac{1}{\rho} \left(\frac{\partial \rho}{\partial T} \right)_P. \tag{5}$$

Making a linear approximation for β:

$$\beta \approx -\frac{1}{\rho_0} \frac{\rho - \rho_0}{T - T_0} \tag{6}$$

where ρ_0 and T_0 are the reference density and temperature. Solving for ρ:

$$\rho \approx \rho_0 \left(1 - \beta(T - T_0)\right). \tag{7}$$

Dividing Equation 4 by ρ_0 and plugging in Equation 7, we get the momentum equation with Boussinesq approximation:

$$\frac{\partial \mathbf{u}}{\partial t} + (\mathbf{u} \cdot \nabla)\mathbf{u} = -\frac{1}{\rho_0}\nabla \left(p - \rho_0 \mathbf{g} \cdot \mathbf{z}\right) + \nu \nabla^2 \mathbf{u} - \mathbf{g}\beta(T - T_0). \tag{8}$$

We can check the validity of using the Boussinesq approximation for our system. This approximation is valid when density variations are small and can be linearly related to temperature changes:

$$\frac{\Delta\rho}{\rho_0} = \beta(T - T_0) \ll 1. \tag{9}$$

Plugging in our β and ΔT values, we get 0.0014. The Boussinesq approximation is valid for our laminar natural convection system.